

## 2 Quantifying NO<sub>x</sub> emissions in Egypt using TROPOMI observations

3 Anthony Rey-Pommier<sup>1</sup>, Frédéric Chevallier<sup>1</sup>, Philippe Ciais<sup>1</sup>, Grégoire Broquet<sup>1</sup>, Theodoros  
4 Christoudias<sup>2</sup>, Jonilda Kushta<sup>2</sup>, Didier Hauglustaine<sup>1</sup> and Jean Sciare<sup>2</sup>.

5 <sup>1</sup> Laboratoire des Sciences du Climat et de l'Environnement, LSCE/IPSL, CEA-CNRS-UVSQ, Université Paris-Saclay,  
6 91190 Gif-sur-Yvette, France

7 <sup>2</sup> The Cyprus Institute, Climate and Atmosphere Research Center, 2121 Nicosia, Cyprus

8 **Correspondence:** Anthony Rey-Pommier (anthony.rey-pommier@lscce.ipsl.fr)

9 **Abstract.** Urban areas and industrial facilities, which concentrate ~~most~~ the majority of human activity and industrial  
10 production, are major sources of air pollutants, with serious implications for human health and global climate. For  
11 most of these pollutants, emission inventories are often highly uncertain, especially in developing countries. Spaceborne  
12 ~~observations~~ measurements from the TROPOMI instrument, onboard the Sentinel-5 Precursor satellite, are used to  
13 ~~measure~~ retrieve nitrogen dioxide (NO<sub>2</sub>) ~~slant column densities with a~~ column densities at high spatial resolution.  
14 Here, we use two years of TROPOMI retrievals to map nitrogen oxides (NO<sub>x</sub> = NO + NO<sub>2</sub>) emissions in Egypt  
15 with a top-down ~~model based on~~ approach using the continuity equation in steady state. Emissions are expressed as  
16 the sum of a transport term and a sink term representing the three-body reaction comprising NO<sub>2</sub> and ~~OH~~ hydroxyl  
17 radical (OH). This sink term requires information on the lifetime of NO<sub>2</sub>, which is calculated with the use of the  
18 CAMS near-real-time temperature and ~~hydroxyl radical (OH)~~ OH concentration fields. ~~The applicability of the~~  
19 ~~OH concentration field is evaluated by comparing the lifetime it provides~~ We compare this derived lifetime with the  
20 lifetime inferred from the fitting of NO<sub>2</sub> line density profiles in large plumes with an exponentially modified Gaussian  
21 function. This comparison, which is conducted for ~~39~~ different samples of NO<sub>2</sub> patterns above the city of Riyadh,  
22 provides information on the reliability of the CAMS near-real-time OH concentration fields; ~~It~~ it also provides the  
23 location of the most appropriate vertical level to represent typical pollution sources in industrial areas and megacities  
24 in the Middle East region. In Egypt, total ~~derived~~ emissions of NO<sub>x</sub> are dominated by the sink term. ~~However,~~ but  
25 they can be locally dominated by wind transport, especially along the Nile where human activities are concentrated.  
26 Megacities and industrial regions clearly appear as the largest sources of NO<sub>x</sub> emissions in the country. Our top-down  
27 model ~~produces emissions whose annual variability~~ infers emissions with a marked annual variability. By looking at the  
28 spatial distribution of emissions at the scale of different cities with different industrial characteristics, it appears that  
29 this variability is consistent with ~~the~~ national electricity consumption. ~~It is also able to~~ We detect lower emissions on  
30 Fridays, which are inherent to the social norm of the country, and ~~to~~ quantify the drop in emissions in 2020 due to  
31 the COVID-19 pandemic. Overall, our estimations of NO<sub>x</sub> emissions ~~estimates~~ for Egypt are ~~found to be~~ 25.07.0%  
32 higher than the CAMS-GLOB-ANT\_v4.2 inventory, ~~but and~~ significantly differ in terms of seasonality.

33

### 34 1 Introduction

35 Economic growth in developing countries has led to a strong increase of urban air pollution (Baklanov et al., 2016 [1]).  
36 Among the different pollutants, nitrogen oxides are key species. They are generally the products of fuel combustion,  
37 such as the ~~combustion~~ burning of hydrocarbons in the air at high temperature. The main sources of these compounds  
38 are ~~therefore~~ vehicle engines, but also heavy industrial facilities such as power plants, ~~metal smelters and cement~~  
39 ~~plants~~ iron and steel mills (Tang et al., 2020 [2]) and cement kilns (Kim et al., 2020 [3]). Their accumulation in the  
40 lowest layers of the troposphere contributes to the formation of smog and acid rain (Singh et al., 2007 [4]). They also  
41 have a significant effect on human health, as they can cause various respiratory diseases (EPA, US., 2016 [5]). To deal  
42 with these phenomena, national and regional governments generally enact a series of air pollution control strategies,  
43 which typically take the form of bans on certain polluting technologies, with the aim of reducing the concentration of

44 pollutants at the local level to targets that must be achieved within a given timeframe. These strategies, which also  
45 help driving technological innovation, have had a significant effect in Europe (Crippa et al., 2016 [6]).

46 In Egypt, population growth, urbanisation, socio-economic development and the associated increase in the vehicle  
47 fleet led to a major degradation of air quality in the last decades, especially in highly populated areas such as Greater  
48 Cairo and the Nile Delta (Abou El-Magd et al., 2020 [7]) , which gather the majority of the population. The Ministry  
49 of State for the Environment has thus initiated new policies that aim to reduce pollution levels throughout the country,  
50 through technical mitigation of emissions, emission standards for vehicles and intersectoral collaboration (UNEP, 2015  
51 [8]). However, Egypt, like most developing countries, such as Egypt, lack lacks the local infrastructure to access detailed  
52 information on technical factors such as energy consumption , or fuel type and technology, leading to discrepancies in  
53 inventories (Xue et al., 2012 [9]). As a consequence, the monitoring of emissions, which is important to evaluate the  
54 effects of ~~the~~ air pollution control policies, is of limited reliability.

55 To overcome the uncertainties in the emission inventories, the use of independent observations systems is becoming  
56 increasingly prevalent. In this study, we investigate the use of satellite remote sensing of atmospheric concentrations to  
57 improve the quantification of NO<sub>x</sub> emissions in Egypt. Spectrally resolved satellite measurements of solar backscattered  
58 radiation enable the quantification of NO<sub>2</sub> and other trace gases absorbing in the UV-Visible spectral range based  
59 on their characteristic spectral absorption patterns. Tropospheric vertical column densities, i.e. vertically integrated  
60 NO<sub>2</sub> concentrations in the troposphere, have been providing information on the spatial distribution of tropospheric  
61 NO<sub>2</sub> at global scale for nearly 30 years, allowing the identification of different sources of NO<sub>x</sub> and the quantification  
62 of the associated emissions (Leue et al., 2001 [10]; Martin et al., 2003 [11]; Mijling and van der A, 2012 [12]; de Foy et  
63 al., 2015 [13]; Goldberg et al., 2019 [14]; Beirle et al., 2019 [15]; Lorente et al., 2019 [16]; Lange et al., 2021 [17]). In  
64 October 2017, the Sentinel-5 Precursor satellite was launched. Its main instrument is the TROPOspheric Monitoring  
65 Instrument (TROPOMI), which provides tropospheric NO<sub>2</sub> column densities at ~~a~~ high spatial resolution , with a large  
66 swath width and with a daily frequency (Veeffkind et al., 2012 [18]). By applying the steady-state continuity equation  
67 (Beirle et al., 2019 [15]; Lama et al., [19], 2020), it is possible to build a top-down model that directly quantifies NO<sub>x</sub>  
68 emissions from these NO<sub>2</sub> column densities, provided that some key parameters (wind, temperature, hydroxyl radical  
69 concentration and concentration ratio between NO<sub>x</sub> and NO<sub>2</sub>) are correctly estimated. This model is used to quantify  
70 the anthropogenic NO<sub>x</sub> emissions in Egypt for a 2-year period, from November 2018 to November 2020.

71 This paper is organised as follows: Section 2 provides a description of the datasets used in this study. Section 3  
72 explains the build-up and the limits of the top-down model approach used to quantify NO<sub>x</sub> emissions in Egypt. It also  
73 presents a method for validating the ~~parameters of the model~~ model parameters by using NO<sub>2</sub> line density profiles  
74 over Riyadh, Saudi Arabia. Section 4 presents the analysis of this validation method. It presents the location of the  
75 main NO<sub>x</sub> sources in Egypt and evaluates the vertical sensitivity of the model. It also assesses the ability of the model  
76 to show less human activity on Fridays and during the lockdown that took place during the COVID-19 pandemic.  
77 It finally confronts the inferred emissions with different inventories in terms of amplitude and seasonality. Section 5  
78 presents our conclusion and general remarks.

## 79 2 Instrumentation and data

### 80 2.1 TROPOMI NO<sub>2</sub> retrievals

81 The TROPOspheric Atmosphere Monitoring Instrument (TROPOMI), onboard the European Space Agency’s (ESA)  
82 Sentinel-5 Precursor (S-5P) satellite, provides measurements for atmospheric composition. TROPOMI is a spectrom-  
83 eter observing wavelengths in the infrared, visible and ultraviolet light at around 13:30 local time. The UV-Visible  
84 spectral band at 405-465 nm is used to retrieve NO<sub>2</sub>. Other spectral bands are used to observe methane, formalde-  
85 hyde, sulphur dioxide, carbon monoxide and ozone, as well as aerosols and cloud physical properties. The very high  
86 spatial resolution offered by TROPOMI (originally 3.5 × 7 km<sup>2</sup> at nadir, improved to 3.5 × 5.5 km<sup>2</sup> since 6 August  
87 2019) provides unprecedented information on tropospheric NO<sub>2</sub>. Its large swath width (~ 2600 km) enables makes  
88 it possible to construct NO<sub>2</sub> images on large spatial scales. Those images greatly improve the potential for detect-  
89 ing highly localised pollution plumes above the ground, identifying small-scale emission sources but also estimating  
90 emissions from megacities, industrial facilities and biomass burning. We use TROPOMI NO<sub>2</sub> retrievals (Level 2 data,  
91 OFFL stream) from November 2018 to November 2020 over ~~the Middle East and Eastern Mediterranean region~~ Egypt.  
92 We also use them over Saudi Arabia, and more specifically over ~~Egypt and~~ the city of Riyadh, Saudi Arabia. ~~The~~  
93 arid climate of this region to evaluate the reliability of other parameters. This will be explained in Section 3.3. Both  
94 countries have an arid climate, which offers a large number of clear-sky days throughout the year, ~~but also the presence~~

95 ~~of enabling the calculation of monthly averages based on more than 20 observations. They are also the host to many~~  
96 large plumes of pollutants due to ~~a large human concentration~~ high human concentrations along rivers and around  
97 megacities, which allows us to observe high NO<sub>2</sub> ~~concentrations in the region~~ concentration patterns with a high  
98 signal-to-noise ratio. ~~To facilitate data filtering,~~ TROPOMI products provide a quality assurance value  $q_a$ . ~~This~~  
99 ~~value, which~~ ranges from 0 (no data) to 1 (high-quality data). For our analysis of concentrations, we selected NO<sub>2</sub>  
100 retrievals with  $q_a$  values ~~equal to or~~ greater than 0.75, which systematically correspond to clear-sky conditions (Eskes  
101 ~~and Eichmannet al., 2019 [20]). TROPOMI soundings are gridded for this study~~ at a spatial resolution of  $0.1^\circ \times 0.1^\circ$   
102 with daily coverage. This resolution is lower than that of the instrument; the gridding thus provides a grid for which  
103 most NO<sub>2</sub> columns correspond to one or more measurements. The observed plumes remain correctly resolved. Cells  
104 without measurements are infrequent, which facilitates the calculation of derivatives.

## 105 2.2 Wind data

106 The horizontal wind ~~information~~  $\mathbf{w} = (u, v)$  is taken from the European Centre for Medium-Range Weather Forecasts  
107 (ECMWF) ERA5 data archive (fifth generation of atmospheric reanalyses) at a horizontal resolution of  $0.25^\circ \times 0.25^\circ$   
108 on 37 pressure levels (Hersbach et al., 2020 [21]). The hourly values have been linearly interpolated to the TROPOMI  
109 orbit timestamp and re-gridded ~~with to~~ a  $0.1^\circ \times 0.1^\circ$  resolution.

## 110 2.3 CAMS real-time fields

111 The Copernicus Atmospheric Monitoring Service (CAMS) global near-real-time service provides analyses and forecasts  
112 for reactive gases, greenhouse gases and aerosols on 25 pressure levels with a horizontal resolution of  $0.4^\circ \times 0.4^\circ$  and  
113 a temporal resolution of 3 hours (Huijnen et al., 2016 [22]). For the calculation of NO<sub>x</sub> emissions from TROPOMI  
114 observations, we use CAMS concentration fields of nitrogen oxides (NO and NO<sub>2</sub>) and hydroxyl radical (OH). We  
115 also use the CAMS temperature field  $T$ . NO and NO<sub>2</sub> concentrations are used to account for chemical processes  
116 that take place in polluted air. Anthropogenic activities produce mainly NO, which is transformed into NO<sub>2</sub> by  
117 reaction with ozone O<sub>3</sub>. NO<sub>2</sub> is then photolyzed during the day, reforming NO ~~and producing an oxygen atom O~~  
118 (Seinfeld, 1989 [23]). This photochemical equilibrium between NO and NO<sub>2</sub> can be highlighted with the NO<sub>x</sub>:NO<sub>2</sub>  
119 concentration ratio, whose value depends on local conditions, allowing to perform a conversion from NO<sub>2</sub> production  
120 to NO<sub>x</sub> emissions. The reason for the use of OH is different. OH is the main oxidant that controls the ability of  
121 the atmosphere to remove pollutants such as NO<sub>2</sub> (Logan et al., 1981 [24]). It is mainly produced during daylight  
122 hours by interaction between water and atomic oxygen produced by ozone dissociation (Levy, 1971 [25]). In air that  
123 is directly influenced by pollution, ~~the second another~~ source of OH is due to a reaction between NO and HO<sub>2</sub>.  
124 This reaction, referred to as the NO<sub>x</sub> recycling mechanism, ~~illustrate illustrates~~ the nonlinear dependence of the OH  
125 concentration on NO<sub>2</sub> (Valin et al., 2011 [26]; Lelieveld et al., 2016 [27]). Since the OH lifetime is typically of less  
126 than a second, its concentration in the troposphere is very low and difficult to measure. As a consequence, global  
127 analyses, which estimate OH concentrations from other variable species (Li et al., 2018 [28]; Wolfe et al., 2019 [29]),  
128 provide a ~~natural~~ representation for OH concentrations ~~, but~~ with high associated uncertainties. Therefore, the CAMS  
129 OH concentrations are used here to account for the NO<sub>2</sub> oxidation to form nitric acid (HNO<sub>3</sub>), whose representation  
130 is explained in Section 3.1. Finally, the temperature field is used to control variations in the kinetic parameters  
131 (Burkholder et al., 2020 [30]). The hourly values are also linearly interpolated to the TROPOMI orbit timestamp and  
132 re-gridded ~~with to~~ a  $0.1^\circ \times 0.1^\circ$  resolution.

## 133 2.4 ~~Calculation of urban enhancements~~ Background removal

134 Detecting traces of anthropogenic emissions in TROPOMI NO<sub>2</sub> images is not a straightforward process. The NO<sub>2</sub>  
135 signal from a sparsely populated area or a small industrial ~~plant facility~~ may be covered by numerical noise or by  
136 the signal generated by natural ~~sources such as lightning (Boersma et al., 2005 [31])~~ NO<sub>x</sub> emissions. In the absence  
137 of anthropogenic sources, TROPOMI observes NO<sub>2</sub> concentrations which constitute a tropospheric background of  
138  $\sim 0.5 \times 10^{15}$  molecules.cm<sup>-2</sup>. At the global scale, this background is the result of different sources. In the lower  
139 troposphere, natural NO<sub>x</sub> emissions are mostly due to fires and soil emissions (Yienger et al., 1995 [32]). It is therefore  
140 necessary to remove the natural part of the atmospheric signal from the detected NO<sub>2</sub> enhancement. ~~, Hoelzemann~~  
141 ~~et al., 2004 [33]). In the upper troposphere however, sources include lightning, convective injection and downwelling~~  
142 ~~from the stratosphere (Ehhalt et al., 1992 [34]), but the factors controlling the resulting concentrations are poorly~~  
143 ~~understood. According to state-of-art estimates, anthropogenic NO<sub>x</sub> accounts for most of the emissions at the global~~  
144 ~~scale, whereas natural emissions from fires, soils and lightning are less significant at the global scale and do not exceed~~  
145 ~~a share of 35% combined (Jaeglé et al., 2005 [35]; Müller and Stavrakou, 2005 [36]), although associated errors can~~

146 be very high. In eastern China, the non-anthropogenic share of total  $\text{NO}_x$  emissions is variable but does not exceed  
 147 20% (Lin, 2012 [37]). Egypt being a desertic region and not very conducive to lightning, we expect the share of those  
 148 non-anthropogenic emissions to be smaller. To estimate anthropogenic  $\text{NO}_x$  emissions, it is therefore necessary to  
 149 remove this share.

150 With an atmospheric lifetime of about a few hours, the presence of  $\text{NO}_2$  is relatively short. Consequently, the  
 151 majority of  $\text{NO}_2$  is not transported far downwind from its sources. Thus, near-surface  $\text{NO}_2$  concentrations are generally  
 152 high over industrial facilities and densely populated areas that need to be identified. Because Egypt's population is  
 153 almost entirely located along the Nile River and its delta, the study of  $\text{NO}_x$  emissions in this country cannot therefore  
 154 be reduced to the study of a small number of point sources, as it would be the case for several other parts of the  
 155 Middle East region, and must be carried out in the form of a mapping of the country. Further explanation-discussion  
 156 is provided in Section 3.3. To identify urban or industrial areas in Egypt, we use the Socioeconomic Data and Applications  
 157 Center (SEDAC) GRUMP (Global Rural-Urban Mapping Project) data archive, which comprises eight global datasets,  
 158 including a population density grid provided at a resolution of 30 arc seconds, with population estimates normalised  
 159 for the year 2000 (CIESIN, 2019 [38]). We combine this database with field data giving the location of industrial  
 160 facilities from energy-intensive industries in the region (data have been retrieved from the Global Energy Observatory  
 161 for oil and gas-fired power plants, from IndustryAbout for aluminium, steel and iron plants and iron smelters, from  
 162 the work of Elvidge et al., 2016 [39] for flaring sites, and from the work of Steven J. Davis and Dan Tong for cement  
 163 plants; links are given; links at the end of this article).

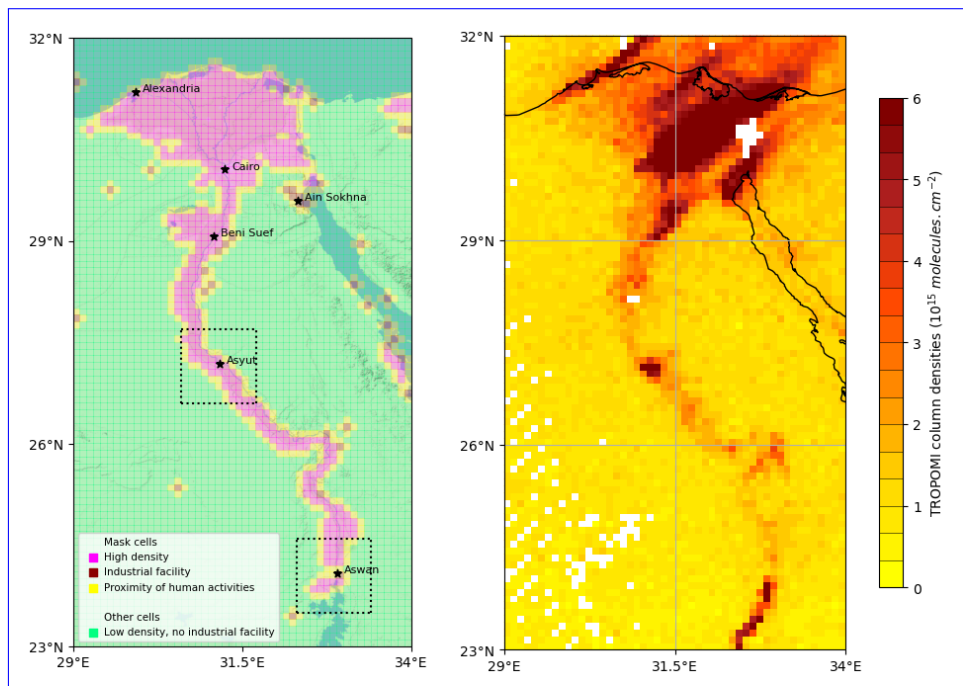


Figure 1: (left) Part of Egypt centered on Nile river. Pink cells represent locations with an average human density above  $100 \text{ hab.km}^{-2}$ , brown cells represent locations with industrial facilities outside cities, and yellow cells represent locations in the vicinity of pink and brown. These cells constitute the mask used to calculate anthropogenic emissions. Green cells represent areas which do not correspond to any of the three criteria, considered to be void of human activity. Five large cities in the country and the industrial area of Ain Sokhna are denoted with stars. Two smaller domains centered around the cities of Asyut and Aswan are represented with dotted lines; their use is presented in Section 4.6. (right) TROPOMI observation of  $\text{NO}_2$  slant column densities above Nile valley on 3 January 2019. White pixels correspond to areas with low quality data ( $q_a < 0.75$ ) or no data.

164 These datasets are used to remove the non-anthropogenic part of the  $\text{NO}_x$  emissions signal. We conduct this removal  
 165 by subtracting the mean emissions over desert and rural areas without human activity from the mean emissions  
 166 over urban and industrial industrial and densely populated areas. In order to perform this distinction between these  
 167 two types of areas, our study is carried out using a grid with a resolution of mask within a  $0.1^\circ \times 0.1^\circ$  characterised  
 168 by two types of cells. A grid cell is considered "urban" to be part of the mask if it has a population density  
 169 higher than a threshold of  $100 \text{ hab.km}^{-2}$ , or if its centre is close to an industrial facility. Otherwise, the cell is  
 170 considered to be part of the "rural background", i.e. outside the mask. In order to avoid any smearing that would  
 171 correspond to abnormally high emissions outside urban areas and industrial centres (which can happen if the wind is

172 poorly estimated), transition cells (in the immediate vicinity of the mentioned urban-mask cells) are also considered  
 173 to be urban-mask cells. Figure 1 shows the distinction between urban-and-rural-mask cells and background cells on our  
 174 domain in Egypt that lies between parallels 23°N and 32°N and meridians 29°E and 34°E. Most urban-of-the-mask cells  
 175 are located in the Nile area. Some urban-mask cells are also found on the coast or in isolated parts in the desert. They  
 176 correspond to remote industrial facilities, including major flaring sites, or sparsely populated industrial centres such  
 177 as Ain Sokhna’s industrial area. The domain comprises  $n_{rur} = 3692$  rural cells and  $n_{urb} = 949$  urban  $n_m = 949$  mask  
 178 cells and  $n_b = 3692$  background cells. The resulting grid is conveniently used as a mask for the urban enhancement,  
 179 whose calculation is explained-mathematical description of the background removal is outlined in Section 3.4.

## 180 2.5 Emission inventories

181 We compare TROPOMI-derived NO<sub>x</sub> emissions to the Emissions Database for Global Atmospheric Research  
 182 (EDGARv5.0) for 2020 and the CAMS global anthropogenic emissions (CAMS-GLOB-ANT\_v4.2) inventory released  
 183 in 2020. Both datasets provide 0.1° × 0.1° gridded emissions for different sectors on a monthly basis. EDGARv5.0  
 184 (Crippa et al., 2019 [?]) is emissions are based on activity data (population, energy production, fossil fuel extraction,  
 185 industrial processes, agricultural statistics, etc.) derived from the International Energy Agency (IEA) and the Food  
 186 and Agriculture Organization (FAO), corresponding emission factors, national and regional information on technol-  
 187 ogy mix data and end-of-pipe measurements. The inventory covers the years 1970-2015. CAMS-GLOB-ANT\_v4.2  
 188 (Granier and differs from the previous version EDGARv4.3.2 which does not use splitting factors derived from the  
 189 Energy Information Administration (EIA) data on fuel consumption of coal, oil and natural gas for specific countries  
 190 (Crippa et al., 2019 [40])2020 [41]). CAMS-GLOB-ANT\_v4.2 is developed within the framework of the Copernicus  
 191 Atmospheric Monitoring Service Its (Granier et al., 2019 [40]). For this inventory, NO<sub>x</sub> emissions are based on  
 192 various existing sectors in the EDGARv4.3.2 emissions from 2000-2012 which are used as a basis for 2010 emissions  
 193 and are extrapolated to the current year using 2011-2014 sector-based trends from the Community Emissions Data  
 194 System (CEDS) inventory (Hoesly et al., 2018 [42]). From one inventory to another, the names and definitions of  
 195 the sectors may vary. In EDGARv5.0 and CAMS-GLOB-ANT\_v4.2, the emissions for a given country are derived  
 196 from the type of technologies used, the dependence of emission factors on fuel type, combustion conditions, as well as  
 197 activity data and low resolution emission factors (Janssens-Maenhout et al., 2019 [43]).

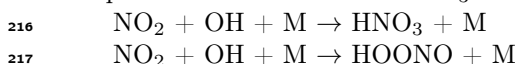
## 198 3 Method

### 199 3.1 Calculation of NO<sub>2</sub> production from TROPOMI observations

200 As a first step, we use TROPOMI’s-tropospheric NO<sub>2</sub> columns-vertical column densities  $\Omega_{NO_2}$  to derive top-down  
 201 NO<sub>2</sub> production maps. Vertical column densities  $\Omega_{NO_2}$  are obtained from TROPOMI slant column densities using an  
 202 air mass factor (AMF) which is also provided by TROPOMI. Previous studies have shown that the use of the AMF is  
 203 a source of structural uncertainty in NO<sub>2</sub> retrievals (Boersma et al., 2004 [44]; Lorente et al., 2017 [45]). In polluted  
 204 environments, this source of uncertainty becomes non-negligible. Here, the AMF does not vary much temporally  
 205 throughout the studied period, and is around 1.6 for mask cells and around 1.9 for background cells. The difference  
 206 between the two types of cells is probably due to a different albedo between the urban environment and desert areas.  
 207 Using the horizontal wind  $\mathbf{w}$ , the NO<sub>2</sub> flux is given as  $\Omega_{NO_2} \mathbf{w}$ . The divergence of this flux is can be added to the local  
 208 time derivative  $\frac{\partial \Omega_{NO_2}}{\partial t}$  to balance NO<sub>2</sub> sources  $e_{NO_2}$  and sinks  $s_{NO_2}$  according to the continuity equation:

$$\frac{\partial \Omega_{NO_2}}{\partial t} + \text{div}(\Omega_{NO_2} \mathbf{w}) = e_{NO_2} - s_{NO_2} \quad (1)$$

209 In steady state, the time derivative disappears and the mass balance is reduced to three terms. The sources-of-NO<sub>2</sub> can  
 210 production can thus be estimated by taking the combined effect of atmospheric transport losses and the different sinks.  
 211 For the transport term, we calculate numerical derivatives with a fourth-order central-finite difference formula-at-each  
 212 point-scheme for each cell of the domain. For the sink term Moreover, since the local overpass time of TROPOMI  
 213 occurs is in the middle of the day, NO<sub>2</sub> losses are largely dominated by the three-body reaction involving NO<sub>2</sub> and  
 214 OH (Seinfeld, 1989 [23]). Two channels have been identified for this reaction (Burkholder et al., 2020 [30]), leading to  
 215 the production of nitric acid HNO<sub>3</sub> and pernitrous acid HOONO:



218 No corrections are made to the TROPOMI observations. Slant column densities are used as vertical densities. This  
 219 use amounts to neglect the air mass factor, which is a source of structural uncertainty in NO<sub>2</sub> retrievals (Boersma et

220 al., 2004 [44]; Lorente et al., 2017 [45]). In polluted environments, this source of uncertainty becomes non-negligible.  
 221 Rather than calculating the air mass factor, we take this factor into account in the final uncertainty estimates. The  
 222 corresponding uncertainty level is given in Section 4.7. For the OH concentrations that are considered in this region  
 223 ( $1.30\text{--}1.20 \times 10^6$  molecules.cm<sup>-3</sup>), the reactions above follow first order kinetics. The total sink term can therefore be  
 224 calculated as  $s_{\text{NO}_2} = \Omega_{\text{NO}_2}/\tau$  with:

$$\tau = \frac{1}{k_{\text{mean}}(T, [\text{M}]) \cdot [\text{OH}]} + \frac{1}{k_{\text{mean}}(T, [\text{M}]) \cdot [\text{OH}]} \quad (2)$$

225  $\tau$  appears here as the characteristic mixed lifetime of NO<sub>2</sub> in the atmosphere. The value of the reaction rate  
 226  $k_{\text{mean}}$  characterises the reactions between NO<sub>2</sub> and OH and depends on atmospheric conditions  
 227 (temperature  $T$  and total air concentration  $[\text{M}]$ ). We calculate the value of  $k_{\text{mean}}$  using a temperature-dependent  
 228 analytical formula for different pressure ranges (Burkholder et al., 2020 [30]) provide a general expression of this rate  
 229 as a function of both temperature  $T$  and total air concentration  $[\text{M}]$ . Note that although this reaction rate accounts  
 230 for both reactions with OH, the second channel is minor and cannot be considered as a true NO<sub>x</sub> sink, HOONO being  
 231 , because HOONO can be rapidly decomposed back to NO<sub>2</sub> and OH in the lower troposphere (Sander et al., 2011 [46])  
 232 ). The value of  $k_{\text{mean}}$  therefore represents the total loss of NO<sub>2</sub> due to OH and cannot be used to infer HNO<sub>3</sub>  
 233 and HOONO production, with a contribution of the HOONO forming reaction between 5 to 15% under atmospheric  
 234 conditions (Sander et al., 2011 [46]; Nault et al., 2016 [47]). Thus, the NO<sub>2</sub> production can be calculated as the sum  
 235 of a transport term and a sink term:

$$e_{\text{NO}_2} = \text{div}(\Omega_{\text{NO}_2} \mathbf{w}) + \Omega_{\text{NO}_2}/\tau \quad (3)$$

236 The treatment for NO<sub>x</sub> removal is simplified here. In reality, NO<sub>x</sub> concentrations are influenced by other sinks. At  
 237 Stavrou et al., 2013 [48] showed that the reaction between NO<sub>2</sub> and OH forming HNO<sub>3</sub> accounted for 26 to 64% of  
 238 total NO<sub>x</sub> loss at the global scale, the other important sinks are. However, the features of the climate in Egypt during  
 239 daytime hinder many other processes to have a significant effect. The following NO<sub>x</sub> sinks, which can be of notable  
 240 importance at the global scale, are not taken into account here:

241 - NO<sub>2</sub> deposition through the leaf stomata of vegetation. This sink can be significant in forested areas. In Egypt,  
 242 the leaf area index is very low, except in the croplands of the Nile Delta where it is comparable to that of southern  
 243 Europe or the western United States (Fang et al., 2019 [49]), for which the corresponding lifetime was of about 10-100  
 244 h (Delaria et al., 2020 [50]), i.e. about an order of magnitude larger than the lifetimes calculated here. To our  
 245 knowledge, there are no studies focusing on the corresponding lifetimes for croplands, and we therefore do not take  
 246 this sink into account.

247 - NO<sub>x</sub> oxidation by organic radicals to produce of alkyl and multifunctional nitrates (Sobanski et al., 2017  
 248 [51]). This sink increases with the concentration of volatile organic compounds (VOC), whose presence cannot be  
 249 excluded in Egypt. Different models have estimated low biogenic isoprene emissions in the region. These emissions  
 250 are concentrated at the level of the Nile and its delta (Guenther et al., 2006 [52]). They are certainly noticeable and  
 251 higher in summer than in winter, and contrast with the rest of the country, but they remain low compared to other  
 252 regions in the world. They are, for instance, about an order of magnitude lower than in the forested areas of the  
 253 eastern US, where the corresponding sink accounts for between 30% and 60% of the total NO<sub>x</sub> sink (Romer Present  
 254 et al., 2020 [53]). Furthermore, at large NO<sub>2</sub> concentrations (compared to VOC concentrations), the share of this  
 255 sink in the total NO<sub>x</sub> loss is weakened compared to that of HNO<sub>3</sub> (Romer Present et al., 2020 [53]). The effect of  
 256 biogenic emissions of VOC can therefore be considered minor. However, VOC emissions can also be of anthropogenic  
 257 origin, especially in urban areas, where they are difficult to estimate. To our knowledge, there is no study evaluating  
 258 the competition of the two sinks in Egypt or in a region with similar features and we therefore do not account for this  
 259 reaction in our calculations.

260 - NO reaction with HO<sub>2</sub> to produce nitric acid (Butkovskaya et al., 2005 [54]), whose yield is strongly enhanced  
 261 in presence of water vapour (Butkovskaya et al., 2009 [55]);

262 - NO conversion to NO<sub>3</sub>, the latter being in thermal equilibrium with NO<sub>2</sub> and N<sub>2</sub>O<sub>5</sub>;  
 263 - NO<sub>2</sub> reversible reaction with peroxyacetyl radical to produce peroxyacetyl nitrate (Moxim et al., 1996 [56]);  
 264 - NO<sub>2</sub> uptake onto black carbon particles (Longfellow et al., 1999 [57]).

265 Stavrou et al., 2013 [48] has shown that the reaction between NO<sub>2</sub> and OH forming HNO<sub>3</sub> accounted for 26 to  
 266 64% of total NO<sub>x</sub> emissions at the global scale. However, the features of the climate in Egypt during daytime hinder  
 267 many other sinks to significantly take place. Losses due to deposition and the formation of alkyl and multi-functional  
 268 nitrates are thus considered insignificant in Egypt where the forest cover is totally negligible. We also neglect the  
 269 reaction between NO and HO<sub>2</sub>. Here, we neglect this reaction as the corresponding reaction rate is weakened lower  
 270 by a factor 3 to 8 in dry conditions (Butkovskaya et al., 2005 [54]). The formation of

271 ~~- NO conversion to NO<sub>3</sub>, the latter being in thermal equilibrium with NO<sub>2</sub> and N<sub>2</sub>O<sub>5</sub>. This sink, which takes~~  
272 ~~place via heterogeneous processes, which has a significant contribution during nighttime in the Mediterranean region~~  
273 ~~(Friedrich et al., 2021 [58]), is neglected at 13:30 when OH is almost at close to its daily maximum. Similarly, the~~  
274 ~~production of PAN;~~

275 ~~- NO<sub>2</sub> reversible reaction with peroxyacetyl radical to produce peroxyacetyl nitrate (Moxim et al., which peaks in~~  
276 ~~1996 [56]). In the Nile Delta region, PAN concentrations in the lower troposphere are significantly below the global~~  
277 ~~average (Fischer et al., 2014 [59]), suggesting a small yield. Moreover, its production peaks in the late afternoon and~~  
278 ~~early evening (Seinfeld, 1989 ), is neglected [23]). We therefore do not consider this sink in the representation of NO<sub>x</sub>~~  
279 ~~emissions at 13:30. Finally, the uptake of 30;~~

280 ~~- NO<sub>2</sub> uptake onto black carbon particles (Longfellow et al., 1999 [57]). This uptake is of limited amount in the~~  
281 ~~Mediterranean region (Friedrich et al., 2021 [58]).~~

282 All these processes ~~being neglected~~ not being accounted for, the reaction between NO<sub>2</sub> and OH is the only sink  
283 that is considered in our calculations to provide ~~a reliable~~ an indication of NO<sub>x</sub> emissions. Section 4.7 details the  
284 consequences of not considering these various minority sinks on the results.

### 285 3.2 Interpolation to daily average emissions

286 All parameters are evaluated at 13:30 local time, which means that the NO<sub>2</sub> production is calculated ~~for at~~ the same  
287 moment. In Egypt, the maximum and minimum electricity consumption are reached around 20:00 and 6:00 local time  
288 respectively, and inter-daily consumption differences have been weakened by the increasing sales of air conditioning  
289 and ventilation systems in the past decades (Attia et al., 2012 [60]). The ~~national average~~ daily load profiles provided  
290 by the National Egyptian Electricity Holding Company show that the mean daily electricity consumption corresponds  
291 approximately to the consumption at 13:30 in the country (EEHC, 2021 [61]). The difference between the two  
292 quantities being ~~very~~ small both in summer (about +2 to -3%) and winter (about -2 to -6%), we ~~neglect this difference~~  
293 ~~and~~ consider our inferred emissions as representative of the average activity in Egypt at any time of the year. This  
294 assumes that electricity consumption dominates the emissions of the country, or that the other emitting sectors have  
295 a similar daily profile. This can be justified. According to CAMS-GLOB-ANT v4.2, the power sector accounts for  
296 50 to 60% of total NO<sub>x</sub> emissions in Egypt. EDGARv5.0 presents a lower share (40 to 45% of total emissions).  
297 Moreover, for both inventories, the transport sector accounts for the majority of the remaining emissions. According  
298 to the traffic congestion index in Cairo ([https://www.tomtom.com/en\\_gb/traffic-index/cairo-traffic/](https://www.tomtom.com/en_gb/traffic-index/cairo-traffic/)), the congestion  
299 level around 13:30 seems to be slightly higher than during the morning peak, but lower than the during night peak.  
300 Traffic emissions at this moment of the day could therefore be representative of the average traffic emissions as well.

### 301 3.3 Validation of CAMS OH concentration using line density calculations for Riyadh

302 When the transport term is integrated over large spatial scales, it cancels out due to the mass balance in the continuity  
303 equation between NO<sub>2</sub> sources and NO<sub>2</sub> sinks. At first order, the integration of the inferred emissions over the whole  
304 domain (of about ~~450~~490,000 km<sup>2</sup>) thus reflects chemical losses of the sink term. In this term, the NO<sub>2</sub> lifetime  
305 calculation involves the reaction rate ~~k<sub>mean</sub>~~k<sub>mean</sub>, whose annual variability is low due to small changes in Egyptian  
306 midday temperatures throughout the year, and OH concentration, whose annual variability is highly marked. In  
307 Egypt, tropospheric OH concentrations, which are strongly correlated with solar ultraviolet radiation (Rohrer and  
308 Berresheim, 2006 [62]) and NO<sub>x</sub> emissions, are higher in summer than in winter. To ensure an ~~adequate~~ appropriate  
309 representation of the OH field by CAMS data, we select a large number of TROPOMI images characterised by a  
310 homogeneous wind field, in which we calculate the NO<sub>2</sub> lifetime according to Equation (2), where [OH] corresponds to  
311 the near-real-time CAMS data and ~~k<sub>mean</sub>~~k<sub>mean</sub> is calculated with the formula from ~~Burkholder~~ Burkholder et al., 2020  
312 [30]. We compare this value with the lifetime determined by a method initially developed by Beirle et al., 2011 [63],  
313 and expanded by Valin et al., 2013 [64] by introducing a rotation of the image to refine the chemical lifetime. This  
314 method consists in fitting an exponentially modified Gaussian function (EMG) to NO<sub>2</sub> line density profiles. These  
315 profiles correspond to the integrated NO<sub>2</sub> ~~mean value~~ columns along the mean wind direction in the pollution pattern  
316 and centered around the source. They are obtained by rotating TROPOMI images in the mean wind direction and  
317 ~~averaging using~~ the values of the nearest columns in a 100 km<sup>2</sup> area. Line density profiles are generated on a ~~distance~~  
318 span of 300 km. An example is given in Figure 3. Within the average profile, the NO<sub>2</sub> burden and lifetime can be  
319 derived from the parameters that describe the best statistical fit. The EMG model is expressed as follows (Lange et  
320 al., 2021 [17]):

$$\langle \Omega_{\text{NO}_2} \rangle(x|B, A, x_0, \mu, \sigma) = B + \frac{A}{2x_0} \exp\left(\frac{\mu - x}{x_0} + \frac{\sigma^2}{2x_0^2}\right) \operatorname{erfc}\left(-\frac{1}{\sqrt{2}}\left(\frac{x - \mu}{\sigma} - \frac{\sigma}{x_0}\right)\right) \quad (4)$$

321 Here,  $x$  is the distance in the downwind-upwind direction,  $B$  is the  $\text{NO}_2$  background,  $A$  is the total number of  
 322  $\text{NO}_2$  molecules observed in the vicinity of the point source,  $x_0$  is the e-folding distance downwind, representing the  
 323 exponential length scale of  $\text{NO}_2$  decay,  $\mu$  is the location of the apparent source relative to the centre of the point  
 324 source, and  $\sigma$  is the standard deviation of the Gaussian function, representing the length scale of Gaussian smoothing.  
 325 Using a non-linear least squares fit, we estimate the five unknown parameters:  $A$ ,  $B$ ,  $x_0$ ,  $\mu$  and  $\sigma$ . ~~Using the mean~~  
 326 ~~zonal wind module  $\sqrt{w^2}$  of the  $\text{NO}_2$  line density~~ ~~From the mean wind module  $w_{\text{mean}}$  in the~~ domain, the mean effective  
 327  $\text{NO}_2$  lifetime  $\tau_{\text{fit}}$  can be estimated ~~from using~~ the fitted parameters:

$$\tau_{\text{fit}} = \frac{x_0}{\langle \sqrt{w^2} \rangle} \frac{x_0}{w_{\text{mean}}} \quad (5)$$

328 The geography of Egypt does not suit the method described here. The Egyptian population is contiguously concentrated  
 329 along the Nile, which makes it difficult to define point sources isolated from human activity. Furthermore, large  
 330 isolated cities such as Alexandria or Suez are too close to the coast for the wind to be considered homogeneous. We  
 331 therefore use the ~~nearby~~ city of Riyadh, Saudi Arabia (24.684°N, 46.720°E) to perform the comparison between the  
 332 CAMS-induced lifetime and the ~~fit-induced fit-obtained~~ lifetime. Riyadh ~~has been the focus of anterior studies~~ (Valin  
 333 ~~et al., 2013 [64], Beirle et al., 2019 [15]), and~~ is particularly suitable for several reasons. Firstly, Riyadh is a city within  
 334 the latitudinal extend of Egypt (1600 km from Cairo) ~~, has with~~ a climate which is similar to the typical Egyptian  
 335 climate. ~~Second~~ ~~Secondly~~,  $\text{NO}_2$  tropospheric columns over Riyadh are high ( $\sim 9 \times 10^{15}$  molecules.cm<sup>-2</sup>), leading to  
 336 retrievals with a high signal-to-noise ratio. ~~Third~~ ~~Thirdly~~, Riyadh is far from the coast, and its flat terrain makes the  
 337 surrounding wind fields rather homogeneous during most of the year.

338 As the fitting algorithm is very sensitive to any disturbance that might be induced by  $\text{NO}_2$  production from other  
 339 point sources, it is necessary to identify heavy industrial facilities in the area. ~~As~~ Riyadh is also an industrial area,  
 340 ~~many power plants are with several power plants~~ located close to the city centre. Figure 2 shows the location of the  
 341 most important emitters in the region, which include five gas-fired power plants (PP7, PP8, PP9, PP10 and PP14),  
 342 one oil-fired power plant (PP4) and one cement plant (CP). The five gas power plants, with a total capacity of more  
 343 than 10 ~~GWe~~ ~~GW~~, are located in the periphery of the city. These power plants are sufficiently far away from the  
 344 city centre for TROPOMI to distinguish their own emissions from those of Riyadh's centre ~~itself~~ with a resolution of  
 345  $0.1^\circ \times 0.1^\circ$ , which is not the case for CP and PP4 which are located in the city centre. It is therefore appropriate  
 346 to restrict the study of  $\text{NO}_2$  patterns over Riyadh to days for which the emissions from the city centre and those  
 347 from the gas power plants do not ~~mix~~ ~~overlap~~. This is the case when the wind blows steadily and homogeneously in a  
 348 north-south direction. Within about 150 km around the city centre, we thus calculate the average ~~zonal~~ wind given by  
 349 ERA5 and consider the observation as reliable if the mean angle  $\langle \theta \rangle$  of the observations deviates by less than  $40^\circ$   
 350 from the north or the south, with a standard deviation  $\sigma_\theta$  of less than  $36^\circ$ . This condition generally leads to a selection  
 351 of observations with large wind speeds, low winds speeds being often associated with more variable directions. This  
 352 ensures the  $\text{NO}_2$  decay to be dominated by chemical removal and not by the variability of the wind (Valin et al., 2013  
 353 [64]). Finally, we select observations with clear-sky conditions downstream of the flow (with at least 80% downstream  
 354 cells with  $q_a > 0.75$ ).

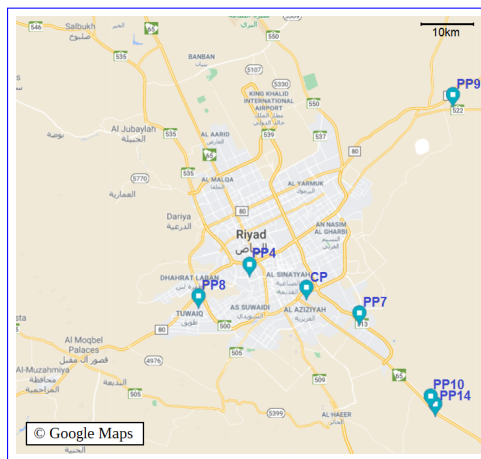


Figure 2: Map of Riyadh's city centre with ~~its~~ ~~the~~ surrounding power plants (PP4, 7, 8, 9, 10 and 14) and cement plant (CP). The map has been extracted from Google Maps.



355 Our  $0.1^\circ \times 0.1^\circ$  gridding ensures that retrieved lifetimes are governed by physical decay of  $\text{NO}_2$  and not an artifact of  
 356 the spatial resolution (Valin et al., 2011 [26]). The fitting procedure is very sensitive to the wind direction. Instead of  
 357 manually correcting the ERA5 wind field for individual  $\text{NO}_2$  patterns, ~~we use another procedure:~~ the curve fitting is  
 358 performed for every sample with three different rotation angles, corresponding to the wind direction with a correction  
 359 of ~~-10, 0 or 10 degrees~~  $-10^\circ, 0^\circ$  or  $10^\circ$ . A record is kept if one of these three fits leads to a ~~determination~~  
 360 with the corresponding  $\text{NO}_2$  line density whose coefficient is greater than 0.97. Among the remaining samples, we  
 361 keep those with a value of  $\tau_{\text{fit}}$  greater than 1.0 hr (considered sufficiently high to be relevant). An example of curve  
 362 fitting is given in Figure 3.

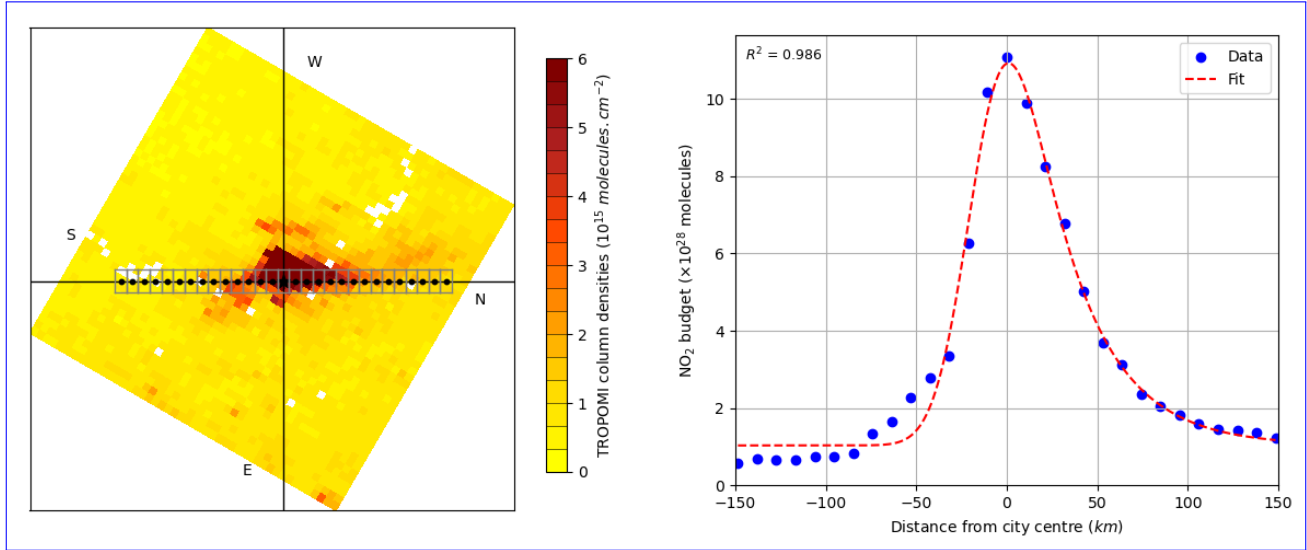


Figure 3: Estimation of the  $\text{NO}_2$  lifetime from a pattern above Riyadh on 03/08/2020 11 March 2020: (left)  $\text{NO}_2$  plume rotated with  
 its wind direction around the source (~~cross star~~) to an upwind-downwind pattern. Grey boxes centered around black points indicate the  
~~spatial extent in extent of~~ the spatial integration of  $\text{NO}_2$  columns to obtain the  $\text{NO}_2$  line density. Values of cardinal points are noted in  
 black. (right) ~~Line Corresponding line~~ densities (points) representing the downwind evolution of  $\text{NO}_2$  as function of the distance to ~~Riyadh~~  
~~Riyadh's~~ city centre, and the corresponding fit according to the exponentially modified Gaussian function (dashed line).

363 The phenomena under study here take place in the planetary boundary layer (PBL), which in this region has  
 364 a midday height of about 2 km (Filioglou et al., 2020 [65]). TROPOMI observations only provide information on  
 365 the total  $\text{NO}_2$  content of the tropospheric column, without providing information on the vertical distribution of  
 366 concentrations. Extracting emissions from concentrations therefore requires a ~~choiee selection~~  
 367 wind, temperature and OH data are taken. Lama et al., 2020 [19] and Lorente et al., 2019 [16] conducted similar  
 368 studies using the boundary layer average wind, while Beirle et al., 2019 [15] chose a vertical level of about 450 m above  
 369 ground. Because vertical transport of  $\text{NO}_x$ , which is emitted mainly from combustion engines and industrial stacks,  
 370 is generally minor compared to horizontal transport,  $\text{NO}_x$  is confined to the first few hundred metres above ground  
 371 level. Using PBL-averaged data poses a problem of consistency as wind, temperature and OH concentration values  
 372 ~~vary significantly significantly vary~~ within the PBL. As a consequence, we compare the CAMS-induced lifetime  $\tau$   
 373 and the fit-induced lifetime  $\tau_{\text{fit}}$  using the parameters ( $\mathbf{w}$ ,  $[\text{OH}]$  and  $T$ ) at two different vertical levels: a medium level  $\mathcal{A}$   
 374 at 925 hPa (about 770 m above ground level), and a bottom level  $\mathcal{B}$  at 987.5 hPa (about 210 m). These levels are  
 375 interpolated from four and two ECMWF or CAMS consecutive pressure levels respectively (1000-850 hPa for level  $\mathcal{A}$   
 376 and 1000-975 hPa for level level  $\mathcal{B}$ ). Most ~~urban mask~~ cells having an altitude between 0 and 150 m, the corresponding  
 377 pressure variations are small (up to  $\sim 16$  hPa), which allows us to neglect the effects of topography on the position of  
 378 pressure levels. Figure 4 sums up the selection method for the comparison of ~~methods~~ lifetimes.

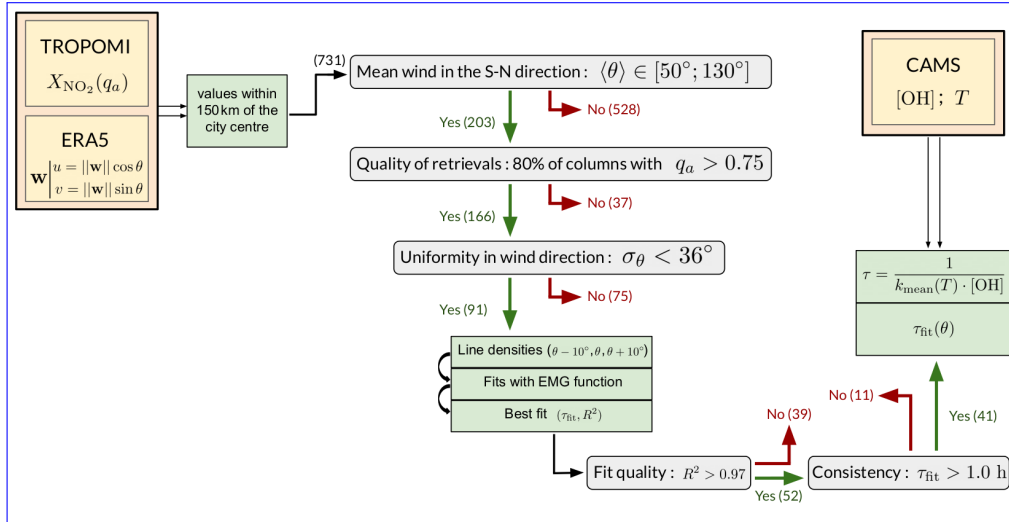


Figure 4: Selection method for  $\text{NO}_2$  patterns over Riyadh. Datasets (yellow-orange) are used to calculate the quantities (light green) that are submitted to different tests (grey). 731 patterns are progressively conserved (green arrows) or rejected (red arrows). At each stage, the number of conserved or rejected patterns are noted within brackets (the value is only given for calculations performed at level B). This selection process compares the lifetimes estimated by the EMG function fitting with TROPOMI line density profiles to the lifetimes calculated according to Equation (2) with CAMS data.

### 3.4 Calculation of anthropogenic $\text{NO}_x$ emissions and comparison with inventories

We calculate  $\text{NO}_x$  emissions on the entire domain from  $\text{NO}_2$  production by using CAMS  $\text{NO}$  and  $\text{NO}_2$  concentrations. These quantities are not intended to replace TROPOMI observations; they are used to apply the concentration ratio  $[\text{NO}_x]/[\text{NO}_2] = ([\text{NO}] + [\text{NO}_2])/[\text{NO}_2]$  to account for the conversion of  $\text{NO}_2$  to  $\text{NO}$  and vice versa. As diurnal  $\text{NO}$  concentrations in urban areas generally range from 2 to 10 ppb to 150 ppb (Khoder, 2008 [66]), the characteristic stabilization time of this ratio ranges from 4 to 20 never exceeds a few minutes (Graedel et al., 1976 [67]; Seinfeld and Pandis, 2006 [68]). This time being lower than the order of magnitude of the inter-mesh transport time (about 30 min considering the resolution used and the mean wind module in the region), we can reasonably neglect the effect of the stabilization time of the conversion factor on the total composition of the emissions and treat each cell of the grid independently from its neighbours. Beirle et al., 2019 [15] found an annual average of 1.32 for this conversion factor, but CAMS data shows small deviations from this value over Egyptian urban areas, as urban concentrations depend on local conditions. We therefore calculate  $\text{NO}_x$  emissions for each cell of the domain the following equations as follows:

$$e_{\text{NO}_x} = \frac{[\text{NO}_x]}{[\text{NO}_2]} e_{\text{NO}_2} \quad (6)$$

For convenience, quantities  $\frac{[\text{NO}_x]}{[\text{NO}_2]} \text{div}(\Omega_{\text{NO}_2} \mathbf{w})$  and  $\frac{[\text{NO}_x]}{[\text{NO}_2]} \Omega_{\text{NO}_2} / \tau$  represent the respective contributions of the transport and the sink terms to total  $\text{NO}_x$  emissions. We finally obtain the emissions related to human activity at the scale of the country  $E_{\text{NO}_x}$  by removing the influence of arithmetic mean value of  $\text{NO}_x$  emissions above background cells from total emissions:

$$E_{\text{NO}_x} = e_{\text{NO}_x} - \frac{1}{n_b} \sum_{i=1}^{n_b} e_{\text{NO}_x, i} \quad (7)$$

These removed emissions are linked to the  $\text{NO}_2$  background detected by TROPOMI and the possible non-anthropogenic sources of estimated by TROPOMI, and do not correspond to anthropogenic emissions. They provide the value of what must be subtracted from the estimates to obtain emissions related to human activity. Such a removal assumes that other processes involved in  $\text{NO}_x$  budgets lead to similar emissions inside and outside the mask, which is not evident, as the majority of background cells are located in the desert or the ocean while the majority of mask cells are located near the Nile River. However, as the processes involved in natural  $\text{NO}_x$  sources lead to emissions much smaller than anthropogenic emissions in polluted areas, we neglect this difference in the following calculations. An alternative would be to calculate an average concentration for the background cells and subtract the corresponding

403 value from the column densities before calculating the emissions. This would pose further reliability problems: for  
 404 instance, very high NO<sub>2</sub> concentrations could appear outside the mask due to wind transport (an example is shown  
 405 on Figure 1). They would lead to an overestimation of the NO<sub>2</sub> background and thus to an underestimation of the  
 406 anthropogenic emissions.

407 Neglecting the part of the country that lies outside the domain, ~~the average surface emissions from Egypt's~~  
 408 ~~anthropogenic activity total emissions from the anthropogenic activity of Egypt can then be obtained by integrating~~  
 409  ~~$E_{\text{NO}_x}$  can be calculated as being the difference between NO<sub>x</sub> emissions over all urban cells and NO<sub>x</sub> emissions over~~  
 410 ~~all rural cells:-~~

$$E_{\text{NO}_x} = \frac{1}{n_{\text{urb}}} \sum_{i=1}^{n_{\text{urb}}} e_{\text{NO}_x,i} - \frac{1}{n_{\text{rur}}} \sum_{j=1}^{n_{\text{rur}}} e_{\text{NO}_x,j}$$

411 on the whole domain. For robust statistics, these derived emissions can be averaged monthly, enabling a month-by-  
 412 month comparison with bottom-up inventories. The linearity of the averaging processes ensures the interchangeability  
 413 of temporal and spatial averages. A monthly average is relevant because it aggregates enough data to limit the high  
 414 inter-day variability due to changing wind patterns or differences between week days and week-ends. In addition, it  
 415 enables the study of monthly NO<sub>x</sub> emission profiles which reflect changes in human activities throughout the year due  
 416 to temperature changes, economic constraints and cultural norms. ~~The use of the average value for rural cells as a~~  
 417 ~~"background" that is subtracted from the emission estimates for urban cells assumes that all natural processes in NO<sub>x</sub>~~  
 418 ~~emissions lead to similar amounts for both types of cells, which is not trivial, as the vast majority of rural cells are~~  
 419 ~~located in desert, mountainous or oceanic areas while the vast majority of urban cells are located near the Nile valley~~  
 420 ~~or the Mediterranean coast. However, as the processes involved in natural NO<sub>x</sub> sources lead to emissions smaller than~~  
 421 ~~anthropogenic emissions in polluted areas (e.g. Lin, 2012 [37] for China), we neglect this difference in the following~~  
 422 ~~calculations. Finally, the total anthropogenic NO<sub>x</sub> emissions of the domain can be obtained by multiplying  $E_{\text{NO}_x}$  by~~  
 423 ~~the cumulative area covered by the urban cells (approximately 95,000 km<sup>2</sup>).~~

## 424 4 Results and discussion

### 425 4.1 Line densities and NO<sub>2</sub> lifetime

426 ~~Here we~~ We compare the results of the TROPOMI line densities fits for Riyadh to the lifetime calculated by Equation  
 427 (2) using CAMS OH data. The two years of TROPOMI observations (from November 2018 to November 2020) provide  
 428 a wide variety of profiles. For level  $\mathcal{B}$ , Figure 4 also provides the number of samples that are being kept at each stage  
 429 of the process. Of the 731 observations available, 203 have a wind direction in the cone with a north-south orientation  
 430 with an aperture of 40° (i.e. between 340° and 20° or between 160° and 200°). Of the remaining observations, 166  
 431 have occurred with a sufficiently clear sky to be retained. The criterion of weak variability for the wind direction brings  
 432 to 91 the number of observations that are kept by the method. On these 91 observations, the line density profiles  
 433 are calculated and the fits applied. According to Equation (5), the lifetime is calculated using the mean wind module  
 434 around the point source. The two lifetimes are calculated with the parameters taken at the medium level  $\mathcal{A}$  or at the  
 435 top level  $\mathcal{B}$ . Of the 91 fits obtained, ~~52-51~~ are of high quality (correlation coefficient between fit function and line  
 436 density profile greater than 0.97) for level  $\mathcal{A}$  and ~~51-52~~ for level  $\mathcal{B}$ . 39 of these fits lead to a lifetime  $\tau_{\text{fit}}$  greater than  
 437 1.0 ~~hr for both levels (they do not necessarily correspond to the same days)~~ h for level  $\mathcal{A}$  and 41 for level level  $\mathcal{B}$ . All  
 438 remaining samples correspond to atmospheric conditions with moderate to fast winds, with a module ranging between  
 439 2 and 11 m/s (with an average of 5.9 m/s) for level  $\mathcal{A}$  and between 3 and 8 m/s (with an average of 5.4 m/s) for level  
 440  $\mathcal{B}$ .

441 These lifetimes are compared to the corresponding lifetimes obtained from CAMS data in Figure 5 ~~for each sample,~~  
 442 which is divided into seasons for a more convenient comparison. The use of level  $\mathcal{A}$  leads to ~~a notable underestimation~~  
 443 notable underestimations of the NO<sub>2</sub> lifetime in autumn compared to the lifetime calculated with the fitting method.  
 444 This same level leads to ~~an overestimation of the lifetime~~ lifetime overestimations in winter. This trend is not found  
 445 with the use of level  $\mathcal{B}$ , which leads to a better reproduction of the lifetimes calculated with the fitting method for the  
 446 available seasons. Figure 5 shows a linear regression between the two calculated lifetimes. The results are scattered,  
 447 with a correlation coefficient higher for level  $\mathcal{B}$  (~~0.3760.408~~) than for level  $\mathcal{A}$  (~~0.1390.220~~). When the intercept of the  
 448 regression line is forced to zero, the resulting slope is closer to 1 for level  $\mathcal{B}$  (~~0.9530.998~~) than for level  $\mathcal{A}$  (~~1.086-~~  
 449 ~~1.071~~).

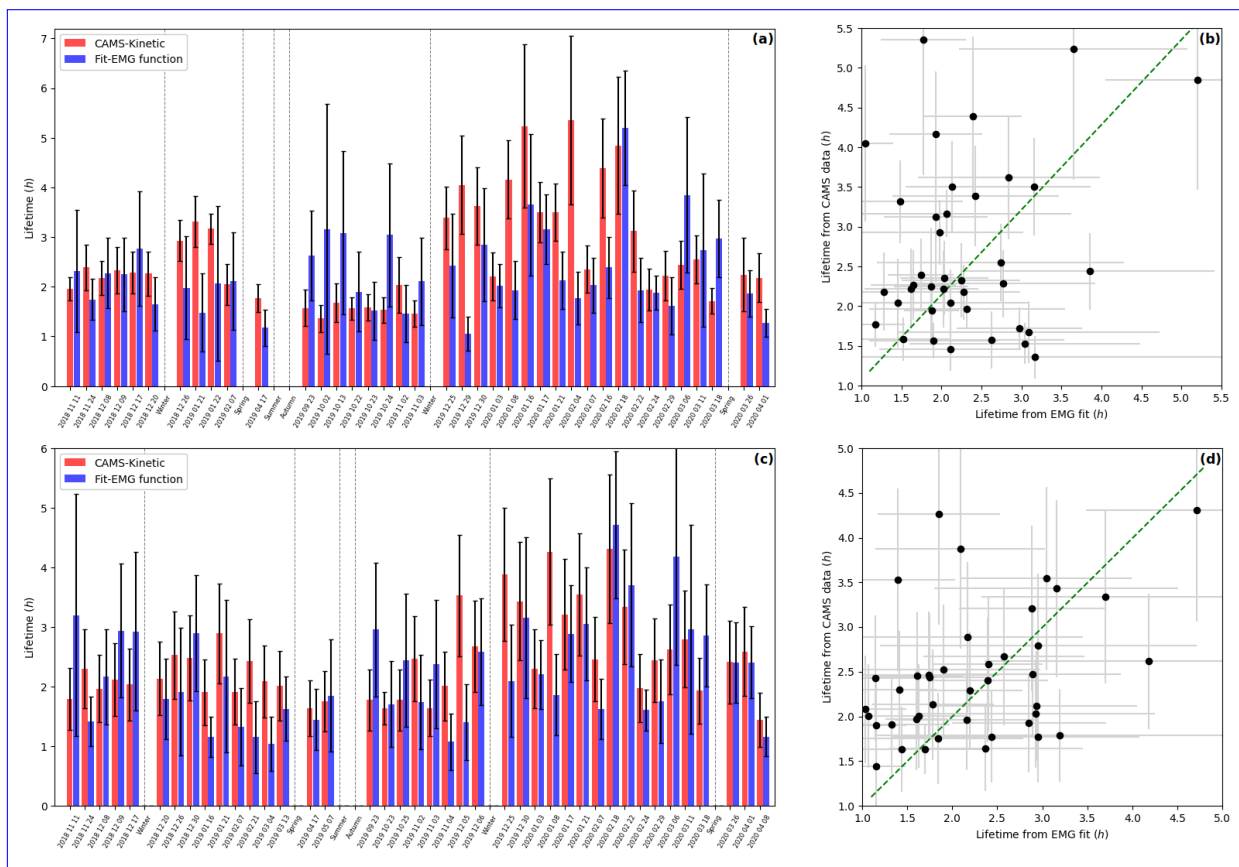


Figure 5: (left) Comparison between CAMS-derived  $\text{NO}_2$  lifetimes and lifetimes from  $\text{NO}_2$  line density fittings with EMG function above Riyadh city centre, for level  $\mathcal{A}$  (a) and  $\mathcal{B}$  (c). The samples presented correspond to patterns in clear-sky conditions for which the mean wind is in the north-south direction with a low variance, and for which the correlation between line density profile and fit gives a correlation coefficient of more than 0.97 and a lifetime of more than 1.0 hrh. ~~No  $\text{NO}_2$  patterns during the summers of 2019 and 2020 meet these conditions~~  $\text{NO}_2$  patterns do not have these conditions during the summers of 2019 and 2020. Dashed lines separate the groups of observations by season. (right) Comparison between the two calculated lifetimes for level  $\mathcal{A}$  (b) and  $\mathcal{B}$  (d). A linear regression with an intercept forced to be zero is displayed with a green dashed line.

450 Level  $\mathcal{B}$  is therefore the one that leads to the best match between the lifetime calculated with Equation (2) and the  
 451 lifetime calculated from line densities. The results that are presented in the following sections (except for Section 4.3)  
 452 are therefore results of calculations performed with parameters ( $\mathbf{w}$ ,  $[\text{OH}]$ ,  $T$  and  $[\text{NO}_x]/[\text{NO}_2]$ ) estimated at level  $\mathcal{B}$ .  
 453 Nevertheless, it should be noted that no summer observations were included in the comparison. The main reason for  
 454 this is the wind direction: of the 188 summer days observed, 178 ~~of them~~ have a mean wind direction outside the  
 455 north-south cone over central Riyadh. On the remaining ten days (one for summer 2019 and nine for summer 2020),  
 456 the ERA5 wind direction is too variable for the fit to be considered relevant, or the fit results in a correlation coefficient  
 457 below 0.97. ~~Thus it~~ It is not clear how correctly the  $\text{NO}_2$  lifetime would be calculated during both summer periods  
 458 by Equation (2). With OH concentrations being the main driver of this lifetime, we cannot assess the relevance of the  
 459 representation of OH concentrations by CAMS data during summer days in the study.

## 460 4.2 Mapping of Egypt's $\text{NO}_x$ emissions

461 The top-down emission model is then applied to the Egyptian domain with CAMS OH concentration and temperature  
 462 fields for lifetime calculations. For each cell,  $\text{NO}_x$  emissions are calculated according to Equation (6), resulting in a  
 463 mapping of Egypt's emissions. The obtained values are averaged monthly from November 2018 to November 2020.  
 464 Figure 6 shows a composition of the emissions map with the transport term and the sink term for the months of January  
 465 and July 2019. The corresponding anthropogenic emissions, calculated according to Equation (7), are added. The  
 466 Nile appears on transport term maps: the divergence calculation complies with what is expected from a line ~~density~~ of  
 467 emitters, i.e. a clear separation of zones of positive divergence from zones of negative divergence with a separation line  
 468 corresponding to the course of the river. The fact that ~~the negative divergence zones are areas of negative and positive~~  
 469 divergence are respectively located to the east ~~of the river and the positive divergence zones to the west and the west~~

470 of the river is the result of the wind being predominantly towards in the northeast and southeast quadrants during the  
 471 overflight of the region zonal component of the wind being positive most of the time. Some point sources like Cairo,  
 472 Alexandria, Asyut or Aswan are easily identifiable. The sink term, directly proportional to the TROPOMI slant  
 473 column densities, also highlights these cities. However, unlike the transport term, which has a similar spatial pattern  
 474 from month to month, the sink term is clearly stronger in summer than in winter. This is mainly due to a higher  
 475 lifetime in winter than in summer ( $4.00\text{ hr}$ – $4.94\text{ h}$  on average in January 2019 and  $2.15\text{ hr}$ – $2.62\text{ h}$  in July 2019) while  
 476 the average TROPOMI  $\text{NO}_2$  concentrations are slightly higher during winter ( $1.687\text{--}1.071 \times 10^{15}$  molecules. $\text{cm}^{-2}$  for  
 477 January 2019 and  $1.440\text{--}0.899 \times 10^{15}$  molecules. $\text{cm}^{-2}$  for July 2019). Over the whole domain, the mean transport term  
 478 varies throughout the studied period between  $-0.035 \times 10^{15}$ – $-0.014 \times 10^{15}$  molecules. $\text{cm}^{-2}.\text{h}^{-1}$  (January–December  
 479 2019) and  $0.026 \times 10^{15}$ – $0.015 \times 10^{15}$  molecules. $\text{cm}^{-2}.\text{h}^{-1}$  (May 2020). Thus, it hardly contributes to the  $\text{NO}_x$  emission  
 480 budget, the mean chemical sink term alone varying between  $0.451 \times 10^{15}$ – $0.223 \times 10^{15}$  molecules. $\text{cm}^{-2}.\text{h}^{-1}$  (January  
 481 2020) and  $1.121 \times 10^{15}$ –December 2019) and  $0.534 \times 10^{15}$  molecules. $\text{cm}^{-2}.\text{h}^{-1}$  (September 2020).

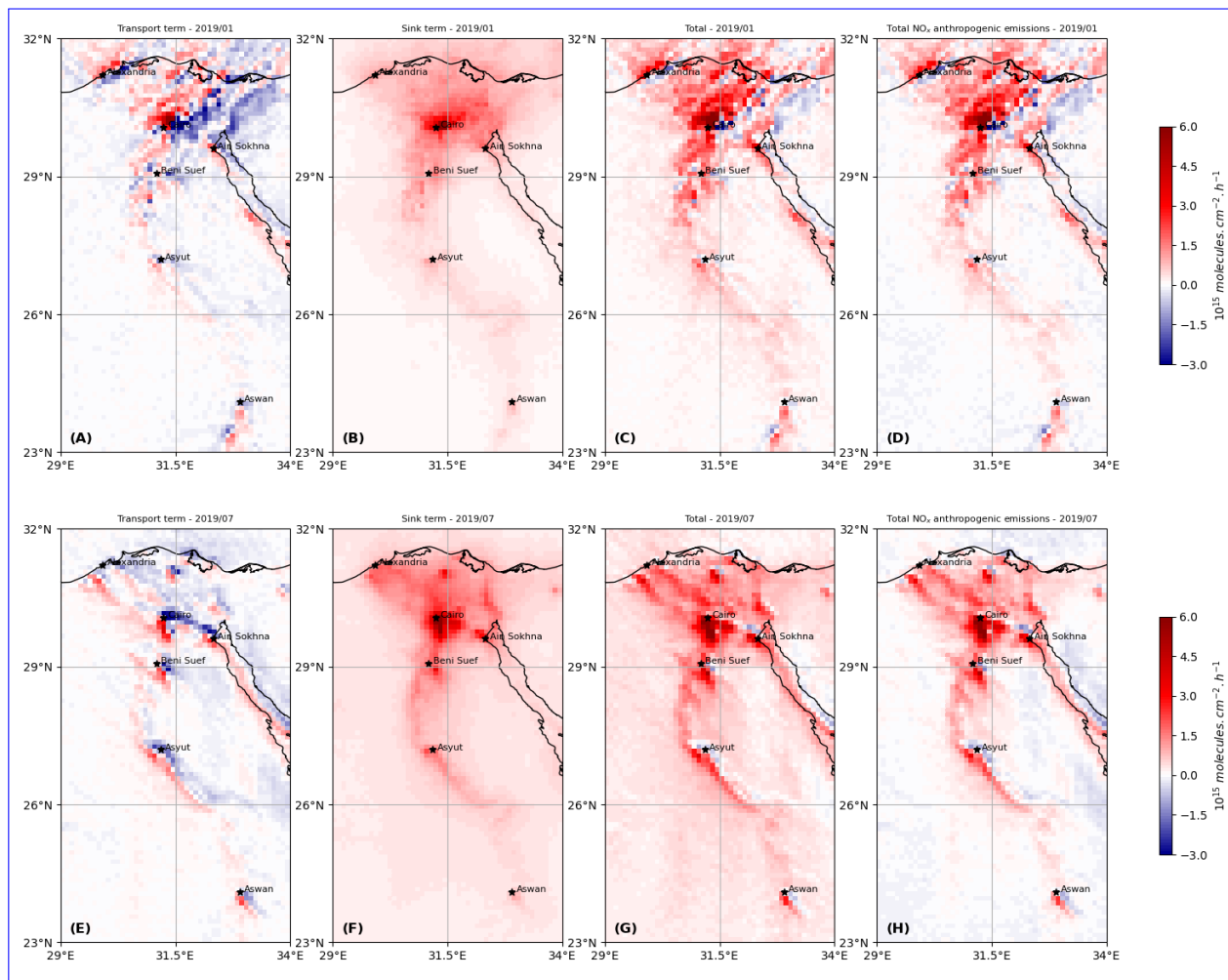


Figure 6: Construction of  $\text{NO}_x$  emissions above most of Egypt's territory: (top) transport term (A), sink term (B) and the resulting surface emissions (C), being counted as total and the corresponding anthropogenic emissions after non-anthropogenic background removal (D) for January 2019. (bottom) transport term (E), sink term (F) and the resulting surface emissions (G), and the corresponding anthropogenic emissions after non-anthropogenic background removal (H) for July 2019.

482 Several cities in the country are thus highlighted appear as the main emitters of the country, such as Cairo, Alexandria,  
 483 Beni Suef, Asyut or Aswan. The industrial area of Ain-Sokhna, located southwest of Suez, also appears as a main  
 484 emitter. Table 1 compares the monthly values for the sink term and the absolute value of the transport term above  
 485 five major cities of the country, with populations ranging from 193200,000 to 19–20 million inhabitants, as well as  
 486 Ain-Sokhna's area. The mean values for TROPOMI column densities are also provided. According to the results,  
 487 the capital city of Cairo is by far the largest emitter in the country, largely due to its large population, resulting in  
 488 high traffic emissions, but also to its intensive industrial activity. Alexandria, the country's second largest city, is not

City	Population density (khab/km <sup>2</sup> )	Jan. 2019			Jul. 2019		
		$\Omega_{NO_2}$	Transport	Sink	$\Omega_{NO_2}$	Transport	Sink
	habitants per square kilometer	$\mathcal{M}_{NO_2} \cdot \text{cm}^{-2}$	$\mathcal{M}_{NO_x} \cdot \text{cm}^{-2} \cdot \text{h}^{-1}$		$\mathcal{M}_{NO_2} \cdot \text{cm}^{-2}$	$\mathcal{M}_{NO_x} \cdot \text{cm}^{-2} \cdot \text{h}^{-1}$	
Cairo	<del>52.2</del> -18,064	<del>18.016</del> -9.415	<del>5.615</del> -2.903	<del>5.520</del> -3.684	<del>8.331</del> -5.618	<del>2.901</del> -2.022	<del>5.883</del> -4.879
Alexandria	<del>3.2</del> -9,133	<del>5.569</del> -3.034	<del>2.047</del> -1.179	<del>1.188</del> -0.975	<del>2.518</del> -1.674	<del>0.694</del> -0.410	<del>2.402</del> -1.421
Asyut	<del>3.0</del> -1,644	<del>4.134</del> -1.708	<del>1.230</del> -0.679	<del>1.298</del> -0.718	<del>4.358</del> -2.137	<del>2.041</del> -1.236	<del>3.110</del> -1.520
Aswan	<del>1.6</del> -319	<del>2.615</del> -0.976	<del>0.431</del> -0.182	<del>1.521</del> -0.473	<del>2.175</del> -0.871	<del>0.555</del> -0.308	<del>1.532</del> -0.520
Beni Suef	<del>2.5</del> -2,056	<del>7.472</del> -2.950	<del>0.974</del> -0.548	<del>2.513</del> -1.080	<del>4.683</del> -2.321	<del>1.571</del> -0.428	<del>4.238</del> -1.590
Ain Sohkna	<del>-(industrial area)</del> -5	<del>8.159</del> -3.133	<del>1.585</del> -1.256	<del>2.548</del> -1.115	<del>5.216</del> -2.56	<del>2.012</del> -1.346	<del>4.737</del> -1.750

Table 1: Comparison between the transport term and the sink term above different cities ~~among the 20 most populous cities~~ in Egypt, as well as the industrial region of Ain Sohkhna located 45 km southwest of Suez for January and July 2019. ~~Numbers TROPOMI vertical NO<sub>2</sub> columns, NO<sub>x</sub> emissions and population densities~~ correspond to average values within 18 km from the city centre. ~~The value for the mean TROPOMI NO<sub>2</sub> column density is also given. The population density of the corresponding governorate (2020 value) is noted as a comparison.~~ Unit  $\mathcal{M}$  stands for a quantity of  $10^{15}$  molecules (NO<sub>2</sub> or NO<sub>x</sub>).

489 necessarily the second largest emitter, as its emissions are comparable to those of smaller cities such as Beni Suef or  
490 Asyut. However, the three cities concentrate a large amount of industrial activity: Alexandria hosts several oil and  
491 gas power plants and a small number of cement factories, while Beni Suef is close to several oil and gas power plants  
492 and hosts several flaring sites. Similarly, the city centre of Asyut is close to ~~two-three~~ oil and gas-fired power plants  
493 and a cement factory. This seems to indicate that industrial activity might be the main ~~factor-cause~~ of NO<sub>x</sub> emissions  
494 differences between these cities, before population size. This explains why NO<sub>x</sub> emissions from these three cities are  
495 comparable to those of the industrial area of Ain Sohkhna, which includes several cement ~~plants-facilities~~, iron smelters  
496 and oil and gas plants. It might also explain why Aswan, which has a population that is comparable to Beni Suef or  
497 Asyut, but which does not have any major industrial site, has slightly lower emissions than the two other cities. ~~An~~  
498 ~~additional analysis of the differences between Asyut and Aswan is provided in Section 4.6.~~ Finally, the Gulf of Suez  
499 displays relatively large emissions, which might be attributed to the shipping sector, the region being a major gateway  
500 for international trade. Because it also hosts several flaring sites, these emissions might also be due to the oil and gas  
501 extraction activity.  
502 Although these cities and areas can be described as high-emission sites, the term responsible for these emissions differ  
503 from one site to the other. Figure 7 shows the contribution of the transport term (taken in absolute value) to total  
504 emissions for January and July 2019. Because wind fields are relatively homogeneous along the Nile on spatial scales  
505 of less than 100 km, NO<sub>2</sub> concentration gradients perceived by TROPOMI in the region mainly contribute to the  
506 increase of the transport term which can reach similar values as the sink term. ~~Conversely, desert~~ ~~However, it is never~~  
507 ~~significantly higher than the sink term: due to a spread of the emissions over large urban areas, the behaviour of these~~  
508 ~~cities is therefore different from that of a point source for which the transport term would be very high (Beirle et al.,~~  
509 ~~2021 [69]).~~

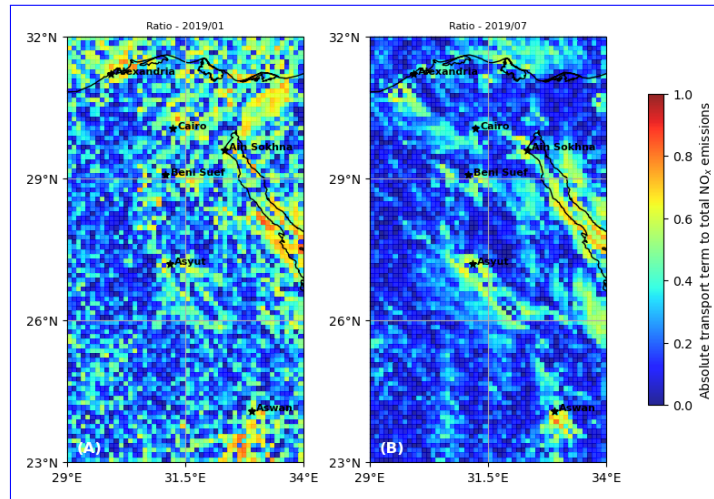


Figure 7: Share of the absolute value of the transport term in the sum of the sink term and the absolute value of the transport term above most of Egypt’s territory, indicating the local importance of the transport term in NO<sub>x</sub> emissions above ~~urban-areas~~~~mask cells~~. The average of this ratio is shown for January 2019 (A) and July 2019 (B).

Desert areas such as the Libyan Desert, the Eastern Desert and the Sinai region, (located respectively to the west, east and northeast of the Nile) show a very low value for the transport term compared to the sink term, due to the homogeneity of both the wind field and the detected NO<sub>2</sub> concentrations in these areas. Finally, a strong predominance of the transport term can be observed near coastal regions even without the presence of emitters nearby due to changing winds.

As a consequence, most cities in the country are characterised by a transport term which can locally be of the same order of magnitude as the sink term, especially during the winter season. In the case of the Gulf of Suez, the transport term can be 1 to 2 times higher than the sink term, which varies between 0.5 and 1.0  $\times 10^{15}$  molecules.cm<sup>-2</sup>.h<sup>-1</sup>. Those values are slightly higher than the average emissions above rural background cells areas due to the sink term (about 0.4–0.6  $\times 10^{15}$  molecules.cm<sup>-2</sup>.h<sup>-1</sup> in winter and 0.7–0.9  $\times 10^{15}$  molecules.cm<sup>-2</sup>.h<sup>-1</sup> in summer). It is also observed that TROPOMI NO<sub>2</sub> column densities above this zone are relatively homogeneous, which indicates that the high value for  $k_{mean}$ , but remain quite low compared to the emissions in large cities. This relative predominance of the transport term is due to abrupt changes in wind direction, which is consistent with the presence of the coast. Consequently, explained by a visible gradient of the TROPOMI NO<sub>2</sub> column densities. The region thus acts as a very thin line of emitters. Nevertheless, this predominance might also be partly due to a poor representation of the wind field by ERA5, caused by the 0.25°  $\times$  0.25° spatial resolution of the data (i.e., the low resolution of ERA-5 (about 26 km in this region, which is the same order of magnitude as the width of the channel) might misestimate the transport term may misrepresent the wind near the coast, creating artificial gradients.

### 4.3 Vertical analysis

Here we investigate the influence of the choice of the vertical level in the representation of the model parameters. This influence is of considerable importance, as NO<sub>x</sub> sources in urban areas can be located at different altitudes. For instance, emissions from the road sector from tailpipes are located at ground level, whereas NO<sub>x</sub> from power plants and industrial facilities can be emitted from stacks, which are usually located between 50 and 300 m above the ground. The results of Section 4.1 results showed that level B was more appropriate for the representation of the NO<sub>2</sub> lifetime. This level is therefore chosen as a reference for the comparison. We study the effect of a transition from level B to level A for each of the 3 parameters involved in the representation of the sink term, i.e. temperature  $T$ , hydroxyl radical concentration [OH] and concentration ratio [NO<sub>x</sub>]/[NO<sub>2</sub>]. The results for the averages over urban and rural areas mask cells and background cells are given for the months of January, April, July and October 2019 in Table 2. As the wind field is only involved in the transport term whose spatial integration nearly leads to zero, the influence of this parameter is not studied.

TITLE		Sink term ( $10^{15}$ molecules.cm <sup>-2</sup> .h <sup>-1</sup> )					
level B (987.5 hPa)	level A (925 hPa)	Jan. 19 (urban-MASK)	Jan. 19 (rural-BKGD)	Apr. 19 (urban-MASK)	Apr. 19 (rural-BKGD)	Jul. 19 (urban-MASK)	Jul. 19 (rural-BKGD)
$T, [OH], \frac{[NO_x]}{[NO_2]}$	-	1.289-0.859	0.493-0.253	1.737-1.072	0.694-0.345	1.969-1.125	0.788-0.376
[OH], $\frac{[NO_x]}{[NO_2]}$	$T$	1.349-0.899 (+4.7%)	0.513-0.264 (+4.2%)	1.827-1.127 (+5.2%)	0.727-0.361 (+4.8-4.6 %)	2.073-1.185 (+5.3%)	0.826-0.394 (+4.9%)
$T, \frac{[NO_x]}{[NO_2]}$	[OH]	0.968-0.769 (-24.9-10.5 %)	0.366-0.219 (-25.7-13.6 %)	-1.013 (-13.4-5.5 %)	0.603-0.324 (-13.1-6.0 %)	1.837-1.129 (-6.7+0.4 %)	0.750-0.375 (-4.8-0.3 %)
$T, [OH]$	$\frac{[NO_x]}{[NO_2]}$	1.310-0.872 (+1.7-1.6 %)	0.499-0.257 (+1.4%)	1.776-1.094 (+2.2-2.1 %)	0.712-0.352 (+2.52.0 %)	1.999-1.143 (+1.5-1.6 %)	0.803-0.383 (+1.9%)

Table 2: Analysis of the effect of a vertical change in the parameters used to estimate the sink term in NO<sub>x</sub> emissions: temperature, hydroxyl radical concentration, and NO<sub>x</sub>:NO<sub>2</sub> concentration ratio. The comparison is conducted between the estimated quantities for level B and level A. The comparison is conducted for mask cells (MASK) and background cells (BKGD) for four months of the year 2019. Values within brackets represent the variation from the base case for which all quantities are estimated at level B.

The transition to the level A generally results in a decrease in temperature, leading to an increase in the reaction rate  $k_{mean}$  and thus an increase in the emissions from the sink term. This transition has only a small influence on the total NO<sub>x</sub> emission estimates, with the total mask and background cells emissions increasing by 4 to 6%. The effect is slightly more pronounced in urban areas, due to a steeper vertical temperature profile in these areas. The influence of OH goes in the opposite direction: its concentration decreases strongly with altitude, weakening the sink term. The share of emissions due to the sink term being proportional to this parameter, the effect of the vertical is very pronounced. Thus, the transition to level A weakens the sink term by 4 to 9% in summer (with an average of -6.03% for  $k_{mean}$ ). This weakening is particularly visible during winter months, for which the emissions are lower by up to 14%. In summer however, the months June/July/August) and by 9 to 26% in winter (with an average of -15.70% for the

549 months December/January/February). This weakening seems more pronounced over urban areas than over rural areas  
 550 from March to October, and more pronounced over rural areas than over urban areas during the rest of the year  
 551 effect is hardly noticeable. Finally, the influence of the NO<sub>x</sub>:NO<sub>2</sub> ratio is negligible on the NO<sub>x</sub> emission estimates. Thus,  
 552 the transition to level  $\mathcal{A}$  results in an increase in the sink term of 2-1 to 4%, due to a decrease in both concentrations  
 553 of NO and NO<sub>2</sub> with respect to the vertical but with a greater decrease for NO<sub>2</sub>. This vertical study confirms the  
 554 crucial importance of the OH concentration representation for the accurate representation of NO<sub>x</sub> emissions. ~~OH~~  
 555 concentration—It appears here as the crucial-an important driver of the sink term, which is much more sensitive to  
 556 vertical differences than temperature or the NO<sub>x</sub>:NO<sub>2</sub> concentration ratio.

#### 557 4.4 Weekly cycle

558 In Egypt, the official rest day is Friday, and the economic activity of the country is *a priori* lower during this day than  
 559 during the other days of the week. We therefore try to characterise this feature, by evaluating the weekly cycle of  
 560 NO<sub>x</sub> emissions. We use the TROPOMI-inferred emissions to obtain averages per day of the week. We use the quality  
 561 assurance  $q_a$  of TROPOMI retrievals to ignore the days for which more than 20% of the domain has low-quality data  
 562 (this happens 43 times in 2018/2019 and 28 times in 2019/2020). Such a filtering avoids accounting for the days when  
 563 a large part of the urban and industrial areas are covered by clouds. However, it misses situations where small clouds  
 564 are localised over large emitters, in which case the corresponding emissions are under-estimated. Figure 8 shows the  
 565 resulting daily emissions for the period November 2018 - November 2019 and November 2019 - November 2020. NO<sub>x</sub>  
 566 emissions are expressed in mass terms as NO. A Friday minimum is observed, defining a marked-weekly cycle. This  
 567 trend is also observed for mean NO<sub>2</sub> column densities, for which no intra-weekly variation is observed. Over the 2018-  
 568 2019 period, Fridays have average emissions of 0.978 ± 0.408-0.811 ± 0.408 kt, which is lower than average emissions  
 569 for the rest of the week, which reach 1.279 ± 0.533-0.997 ± 0.533 kt. A similar trend is observed in 2019-2020, for which  
 570 the average for Fridays is 0.856 ± 0.357-0.704 ± 0.357 kt and the average for other days is 1.067 ± 0.449-0.921 ± 0.449  
 571 kt. The difference in emissions between the two periods is due to smaller emissions in December 2019, January 2020  
 572 and February 2020 that are discussed in Section 4.5. On average, Friday emissions correspond to a ratio of 0.81-0.83:7  
 573 (i.e. a value of 0.81-0.83 after normalisation on the seven days of the week) for the entire domain. This result is  
 574 consistent with the values obtained by Stavrakou et al., 2020 [70], who used TROPOMI data and another emission  
 575 model to calculate a ratio of 0.71:7 for Cairo and 0.89:7 for Alexandria in 2017.

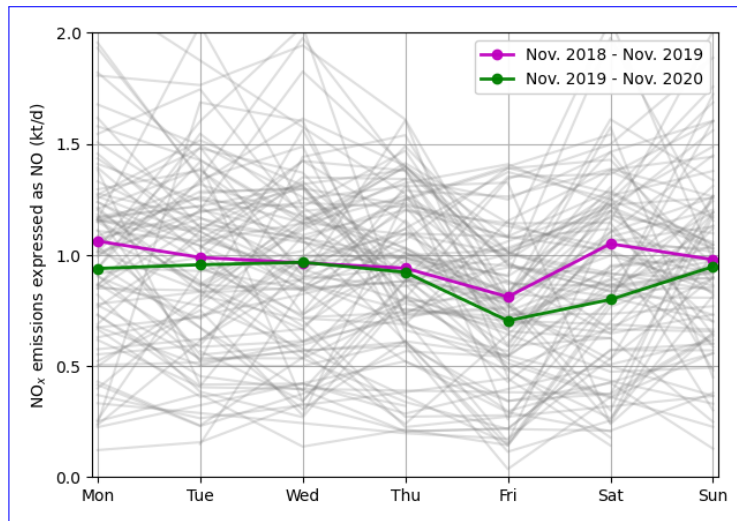


Figure 8: Weekly profiles of anthropogenic NO<sub>x</sub> emissions for Egypt using TROPOMI observations in 2018-2019 (purple line) and 2019-2020 (green line). Thin grey lines represent individual weeks. Days for which less than 80% of the domain counts low quality observations ( $q_a < 0.75$ ) are not represented.

#### 576 4.5 Impacts of lockdown during COVID-19

577 The ongoing global outbreak of COVID-19 forced many countries around the world to implement unprecedented  
 578 public health responses, including travel restrictions, quarantines, curfews and lockdowns. Such measures have helped  
 579 to counter the spread of the virus and have, meanwhile, caused high reductions in global demand for fossil fuels (IEA,  
 580 2020 [71]). They also led to a fall in the levels of NO<sub>2</sub> and other air pollutants across the globe (Venter et al., 2020



581 [72]; Bauwens et al., 2020 [73]; Barré-Gkatzelis et al., 2021 [74][75]. To prevent the spread of COVID-19, Egyptian  
582 authorities ordered a partial lockdown from March 15th till June 30th 2020, closing all public areas (e.g. sport centres,  
583 nightclubs, restaurants and cafes) and suspending religious activities in all mosques and churches throughout the  
584 country. They also implemented more drastic measures such as a full lockdown during Easter (April 20th) and Eid  
585 (May 23rd to May 25th), ~~resulting in~~ before lifting some restrictions on June 1st (Hale et al., 2021 [76]). In addition  
586 to the effect of containment on the activity of the country, the global decline in consumption led to a drop in the  
587 production of certain industrial products.

588 Several studies have estimated the impact of these events on the air pollution levels in the urban centres of the  
589 country : from in-situ measurements, El-Sheekh et al., 2021 [77] estimated that NO<sub>2</sub> concentrations had dropped by  
590 25.9% in Alexandria’s city centre after the start of the lockdown on March 13th, while El-Magd et al., 2020 [78] used  
591 OMI retrievals to estimate a 45.5% reduction of NO<sub>2</sub> concentrations for the entire country during the spring compared  
592 to 2018 and 2019 average values. However, due to a changing lifetime of NO<sub>2</sub>, reductions in the concentrations of  
593 NO<sub>2</sub> might not be entirely due to a ~~drop of decrease in~~ NO<sub>x</sub> emissions, which leads us to focus on the variation of  
594 NO<sub>x</sub> emissions during this singular period. Using our top-down emission model, reductions in total NO<sub>x</sub> emissions of  
595 ~~34.6%, 17.4% and 16.6%~~ 20.1%, 11.8% and 13.5% are observed for the ~~respective~~ months of March, April and May 2020  
596 compared to the equivalent months in 2019. This drop of emissions in 2020 compared to 2019 calculated by the model  
597 also correspond to a decrease in observed NO<sub>2</sub> columns. ~~However, no~~ No significant changes in OH concentrations seem  
598 to appear: on average, from 2019 to 2020, CAMS near-real-time data shows a decrease of 5.5% for OH concentration  
599 over the ~~urban-mask~~ cells for the period March/April/May, while TROPOMI retrievals above ~~urban-areas-mask~~  
600 cells show a decrease in NO<sub>2</sub> column densities of 21.6% over the same period. However, these effects observed for  
601 the months of March, April and May 2020 are not repeated in June 2020, for which emissions show an increase of  
602 ~~12.3%~~ 15.8% compared to June 2019. This ~~increase-rise~~ is largely the result of an increase in the difference between  
603 ~~urban and rural average emissions (as calculated according to Equation 7)~~ average estimates inside and outside the  
604 mask. Indeed, ~~the urban term of emissions within the mask in June 2020 is higher than that are higher than those~~  
605 of June 2019, due to an increase in TROPOMI ~~urban concentrations concentrations above mask cells~~ (+2.47.7%)  
606 while the NO<sub>2</sub> lifetime is almost unchanged (+0.43.3%). ~~The rural term Emissions outside the mask~~ varies in the  
607 opposite direction: a decrease in TROPOMI ~~rural concentrations (-7.6%~~ background concentrations (-5.4%) is observed  
608 while NO<sub>2</sub> lifetime increases strongly (+11.516.0%). This increase in June emissions seems to indicate that the lift  
609 on restrictions allowed a catch-up of the economic activity which ~~has be was~~ sufficiently strong to generate higher  
610 emissions in 2020 than in 2019.

## 611 4.6 Annual cycle and comparison to inventories

612 Here, we attempt to compare our TROPOMI-derived NO<sub>x</sub> emissions to emissions from ~~CAMS and EDGAR~~  
613 CAMS-GLOB-ANT\_v4.2 and EDGARv5.0 inventories. Figure shows the total anthropogenic NO<sub>x</sub> emissions over the  
614 ~~urban-mask~~ cells from November 2018 to November 2020 ~~(i.e. a period of two years), with the average anthropogenic~~  
615 ~~emissions~~, calculated according to Equation (7). As indicated in Section 3.2, the emissions, calculated at 13:30 local  
616 time, are representative of the average daily consumption in Egypt. The total calculated for each month therefore  
617 corresponds to the NO<sub>x</sub> production by human activities in ~~Egyptian urban and industrial areas~~ the country. After  
618 aggregating the different sectors of activity, CAMS and EDGAR inventories directly provide the anthropogenic NO<sub>x</sub>  
619 emissions over the same ~~areas~~ domain. All NO<sub>x</sub> emissions are expressed in mass terms as NO. We note that the  
620 EDGAR inventory does not cover the period 2018-2020 (the ~~inventory ends in last available year of the inventory is~~  
621 2015). On Figure , EDGAR emissions corresponding to the period between November 2013 and November 2015 are  
622 displayed, i.e. ~~with a delay of the preceding~~ 5 years compared to TROPOMI-derived emissions and CAMS estimates.

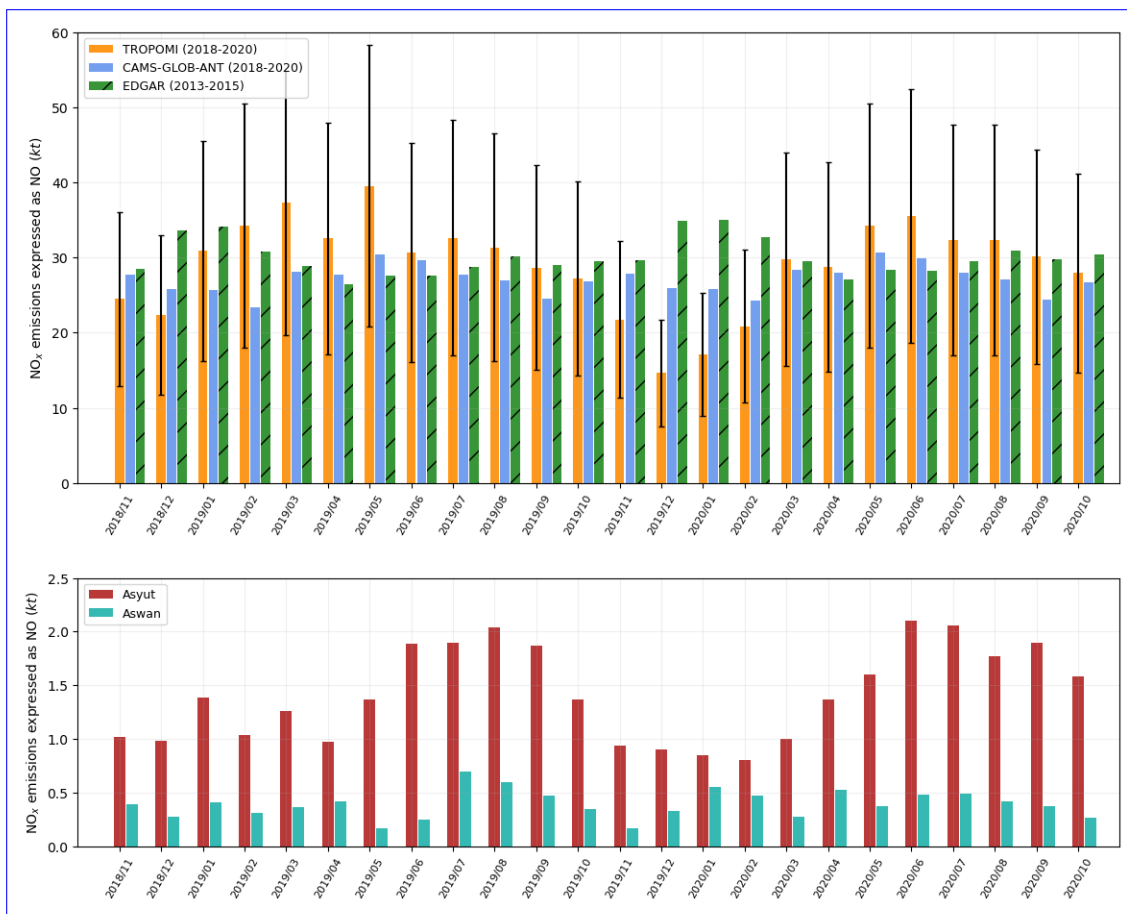


Figure 9: (top) Comparison of TROPOMI-derived anthropogenic NO<sub>x</sub> emissions in Egypt (light blue), with the corresponding emissions from EDGAR (red-green with stripes) and CAMS (yellow) inventories. EDGAR data is provided shown for comparison purposes and covers the years 2013-2015. Error bars for TROPOMI-derived emissions are calculated using uncertainties for the parameters involved in Equation 7. (bottom) TROPOMI-derived anthropogenic NO<sub>x</sub> emissions for the cities of Asyut (dark red) and Aswan (light blue). The corresponding domains are displayed on Figure 1.

623 TROPOMI-derived emissions are lower than the inventory estimates between November 2019 and February 2020.  
 624 higher than the CAMS inventory estimates. The top-down model estimates total emissions of 697.6 kt over the 24  
 625 months, which is 45.9 kt higher than CAMS for the same period (651.6 kt). This difference is primarily localized in  
 626 the first 12 months, for which TROPOMI-inferred emissions are always higher than the inventories and show higher  
 627 values in summer than during the rest of the year. The next 12 months show similar emissions in summer but much  
 628 lower values in winter. In particular, the difference is significant in December 2019 and January 2020 (respectively  
 629 54.8% and 55.756.5% and 66.5% of CAMS levels). These emissions also contrast with other winter emissions, with  
 630 a total of 31.7 kt for 2019-12/2020-01 against 53.3 kt for 2018-12/2019-01 and 57.7 kt for 2020-12/2021-01. In the  
 631 computations, this decrease drop for winter 2019/2020 is mainly due to a relatively low value of the OH concentration  
 632 which reaches  $5.86-4.61 \times 10^6$  molecules.cm<sup>-3</sup> on average for these two months, with 4.95 December 2019 and January  
 633 2020, with  $4.29 \times 10^6$  molecules.cm<sup>-3</sup> above urban areas and 6.09 mask cells and 4.69  $\times 10^6$  molecules.cm<sup>-3</sup> over rural  
 634 areas background cells. They were respectively 6.96, 6.94 and 6.97-5.29, 5.74 and 5.18  $\times 10^6$  molecules.cm<sup>-3</sup> for the  
 635 previous year (December 2018-January 2019) and 7.24, 6.94 and 7.31 2018-12/2019-01) and 5.11, 4.90 and 5.16  $\times 10^6$   
 636 molecules.cm<sup>-3</sup> for the year before (December 2017-January 2018 subsequent year (2020-12/2021-01)). A decrease in  
 637 tropospheric columns (-14.3% for urban areas and -4.6% for rural areas 18.5% for mask cells and -7.6% for background  
 638 cells compared to winter 2018/2019) also contributes to this drop. The accuracy of the inferred emissions for winter  
 639 2019/2020 can therefore be questioned.

640 Except for this singular period, TROPOMI-derived emissions are higher than the CAMS inventory estimates. The  
 641 top-down model estimates total emissions of 814.5 kt over the 24 months, which is 162.9 kt higher than CAMS for the  
 642 same period (651.6 kt). Of these 162.9 kt, 125.2 kt are emitted during the first 12 months (before the underestimation  
 643 period) and 37.7 kt during the 12 following months. The average value for top-down NO<sub>x</sub> emissions are 25.0% higher  
 644 than CAMS estimates. TROPOMI-inferred emissions show an annual variability: the emissions seem to follow At

645 ~~first sight, the annual variability of TROPOMI-inferred emissions, which describes~~ a one-year ~~seasonal cycle where~~  
646 ~~emissions are higher in summer than in winter. These results, at first sight, seem~~ cycle with higher emissions in  
647 ~~summer, seems~~ to be correlated with power emissions which dominate the use of fossil fuels in Egypt (Abdallah  
648 et al., 2020 [79]). These power emissions are due to the country’s residential electricity consumption (Attia et al.,  
649 2012 [60]; Elharidi et al., 2013 [80]; Nassief, 2014 [81]). They also meet the needs of industry. Summer peaks in  
650 electricity consumption are mostly driven by temperature: ~~for instance, the~~, as illustrated by the increasing sales of  
651 air conditioning and ventilation systems ~~have been increasing~~ for several decades (Wahba et al., 2018 [82]). The use  
652 of air conditioning in cars, which requires an additional amount of fuel, could also contribute to the increase of NO<sub>x</sub>  
653 emissions in summer. ~~However, To support this hypothesis, we use our model on two smaller domains centered around~~  
654 ~~the two cities of Asyut and Aswan. The corresponding domains are displayed on Figure 1. Both cities have similar~~  
655 ~~demographic features, with populations of about 467,000 and 315,000 inhabitants in 2021 and human densities of~~  
656 ~~about 3,000 and 1,600 inhabitants per square kilometer respectively. However, their industrial features largely differ.~~  
657 ~~There is no large fossil fuel-fired power plant in Aswan, where most of the electricity is produced by a hydroelectric~~  
658 ~~dam, whereas Asyut counts three oil and gas power plants of various capacities (90, 650 and 1500 MW) in its urban~~  
659 ~~area. Both cities have a cement plant, but the one in Asyut has a larger production capacity (5.7 Mt/yr in Asyut,~~  
660 ~~0.8 Mt/yr in Aswan). Our model is used following the same procedure as for the main domain. The background~~  
661 ~~removal is done at the scale of the country. A seasonal cycle appears for Asyut, with a minimum for winter months~~  
662 ~~and a maximum for summer months. This cycle seems slightly shifted from the one observed for the entire country,~~  
663 ~~for which May emissions are as important as those of summer months. We also note that the decrease in emissions~~  
664 ~~for winter 2019/2020 is less marked than for the emissions of the whole country, and of a similar value to the previous~~  
665 ~~winter. This suggests that national NO<sub>x</sub> emissions are indeed lower during winter, but that the values obtained for~~  
666 ~~winter 2019/2020 are particularly low. We also find that the seasonality of the emissions is more pronounced for the~~  
667 ~~Asyut domain than for the country as a whole. The case of Aswan is different. Emissions within the corresponding~~  
668 ~~domain are significantly lower than for Asyut. The signal-to-noise ratio being higher, it is difficult to characterise an~~  
669 ~~annual cycle, but the results do not seem to indicate low emissions in winter and high emissions in summer. This~~  
670 ~~identification of a seasonal cycle identical to that of the entire country for a city with several power plants, and the~~  
671 ~~absence of such a cycle in a city without any, strengthens the hypothesis that the power sector plays a major role in~~  
672 ~~Egyptian NO<sub>x</sub> emissions.~~

673 ~~We note that~~ some features of the industrial activities in the ~~region-country~~ might be counteracting this trend. For  
674 some sectors such as cement or steel, production is lower in summer, due to the physical wear experienced by workers  
675 due to heat, but also due to certain periods of leave. Given the importance of industrial activities in the production of  
676 NO<sub>x</sub> shown in Section 4.2, this aspect cannot be neglected. The transport sector could also counteract the observed  
677 trend: although the use of air conditioning in cars increase NO<sub>x</sub> emissions of the sector, the observed mean traffic  
678 in the country is higher between November and February and lower between June and August, especially in Cairo  
679 which gathers most of the population. In the absence of additional data, it therefore seems difficult to conclude on  
680 the ~~relevance-amplitude~~ of the seasonal cycle ~~that seems to be~~ produced by our top-down model. This caution is  
681 all the more necessary as CAMS and EDGAR ~~inventories show different seasonal cycles in~~ show seasonal cycles for  
682 NO<sub>x</sub> emissions, with different dynamics ~~than those displayed by TROPOMI emissions~~: while the EDGAR inventory  
683 predicts a maximum of emissions in December or January and a minimum in April, the CAMS inventory shows two  
684 local maxima each year in May and November and two local minima in February and September. The amplitude of  
685 the ~~cycle is higher in EDGAR than in CAMS~~ corresponding cycles is much lower in those inventories, representing  
686 14.2% of the average value for emissions estimates ~~in for~~ EDGAR and 12.4% ~~in CAMS. These differences between~~  
687 ~~the model and the inventories do not give us any information on the seasonality of NO<sub>x</sub> emissions that should be~~  
688 ~~found in the outputs of our top-down model for CAMS. Those values must be compared to the amplitude displayed by~~  
689 ~~TROPOMI-inferred emissions, for which the maximum/minimum ratio is about 1.8 if winter 2019/2020 is excluded,~~  
690 ~~and 2.7 if it is included.~~

#### 691 4.7 Uncertainties and assessments of ~~the previous~~ results

692 The estimation of NO<sub>x</sub> emissions is based on the use of several quantities with varying uncertainties. The error bars  
693 shown in Figures 5 and 9 are thus calculated from uncertainty statistics whose references are presented in this section.  
694 Since these references do not specify the exact nature of these statistics, we assume they correspond to standard  
695 deviations. The uncertainty of tropospheric NO<sub>2</sub> columns under polluted conditions is dominated by the sensitivity  
696 of satellite observations to lower tropospheric air masses, expressed by the tropospheric air-mass factor (AMF). The  
697 ~~AMF depends on the viewing geometry, surface albedo, NO<sub>2</sub> vertical profile, and cloud characteristics (Lorente et al.,~~  
698 ~~2017 [45]; Eskes et al., 2019 [20]). The~~ column relative uncertainty due to the AMF is of the order of 30% (Boersma et

699 al., 2004 [44]). S-5P validation activities indicate that TROPOMI tropospheric NO<sub>2</sub> columns are systematically biased  
700 low by about 30%-50% over cities ([Compernelle et al., 2018 \[83\]](#)), which is most likely related to the *a priori* profiles  
701 used within the operational retrieval that do not reflect well the NO<sub>2</sub> peak close to ground. For the Middle East region,  
702 the impact of the *a priori* profile is less critical, as surface albedo is generally high and cloud fractions are generally  
703 low. Thus, we expect no such bias, and consider a relative uncertainty of 30% for the tropospheric column. Other  
704 uncertainties must be taken into account: the transition from NO<sub>2</sub> TROPOMI columns to NO<sub>x</sub> emissions requires  
705 parameters which appear in Equation (2) and Equation (3). For ~~both zonal and meridional wind components, we~~  
706 ~~assume an uncertainty of wind module, uncertainties are generally of about 1 m/s for components taken at precise~~  
707 ~~altitudes~~ (Coburn et al., 2019 [84]); ~~Beirle et al., 2019 [15]). Here, we assume an uncertainty of 3 m/s for both~~  
708 ~~zonal and meridional wind components.~~ For [OH], the analysis of different methods conducted by Huijnen et al., 2019  
709 [85] showed smaller differences for low latitudes than for extratropics, but still significant. We thus take a relative  
710 uncertainty of 30% for OH concentration. For the reaction rate  $k_{mean}$ , the value of the corresponding relative  
711 uncertainty has been estimated by Burkholder et al., 2020 [30]. ~~Because the sensitivity test conducted~~ Finally, we use  
712 ~~the sensitivity tests performed~~ in Section 4.3 ~~shows that changing the temperature vertically only changes the results~~  
713 ~~by 2-3%, and because vertical temperature gradients are much stronger than horizontal temperature gradients, then~~  
714 ~~the uncertainty related to the horizontal temperature field is small. Therefore, we neglect the impact of temperature~~  
715 ~~on final uncertainty.~~ ~~As a consequence, the~~ to assess the uncertainty associated with the choice of the vertical level.  
716 ~~The cumulative effects on the final emissions of the three parameters studied, in particular the OH concentration, lead~~  
717 ~~to a relative uncertainty that varies from month to month between 7 and 18%. The propagation of these different~~  
718 ~~uncertainties on the monthly estimates of NO<sub>x</sub> emissions in Egypt leads to an expanded uncertainty between 40 and~~  
719 ~~43 and 51%. For lifetimes calculated with the EMG function fitting, the corresponding expanded uncertainty ranges~~  
720 ~~between 18% and 79%.~~

721 We acknowledge the fact that our treatment of ~~uncertainties is simplified there~~ NO<sub>x</sub> is simplified. Many minor sinks  
722 highlighted in Section 3.1 are ~~neglected in the calculations, and the corresponding uncertainty are~~ not taken into  
723 account. ~~Moreover, among the remaining sources of uncertainties, In particular, anthropogenic VOC emissions, which~~  
724 ~~remove NO<sub>x</sub> from the atmosphere, compete with the oxidation by OH for the representation of NO<sub>x</sub> loss. These~~  
725 ~~emissions are difficult to estimate and the corresponding sink is complex to model. Taking this reaction into account~~  
726 ~~would a priori lead to a strengthening of the sink term and thus to an increase of the major ones are treated with~~  
727 ~~fixed values for relative uncertainties, which leads to absolute uncertainties that are roughly proportional to monthly~~  
728 ~~emissions. As a result, the confidence interval displayed on Figure is larger in summer than in winter (with a length~~  
729 ~~of 6.0 kt in January 2020 and of 17.4 kt for July 2020), and the drop in emissions for winter 2019-2020 appears as~~  
730 ~~a persistent feature of the model outputs. If this drop is realistic, then our top-down model provides a method for~~  
731 ~~improving national inventories. If it is not, then several assumptions of our model NO<sub>x</sub> emissions estimates. Other~~  
732 ~~assumptions in the model are also simplifications. For instance, obtaining anthropogenic emissions by subtracting the~~  
733 ~~average emissions over background cells assumes that the non-anthropogenic sources of NO<sub>2</sub> are similar inside and~~  
734 ~~outside the mask, which is not true, since a large part of the mask cells correspond to croplands. For these cells, soil~~  
735 ~~emissions may play a non-negligible role in the natural NO<sub>2</sub> budget. As a consequence, mean background emissions~~  
736 ~~that are removed from NO<sub>x</sub> emissions estimates above mask cells might be under-estimated. Finally, the reliability of~~  
737 ~~the data used can be questioned. For instance, because this drop~~ The representation of the wind is crucial to avoid  
738 ~~creating artificial patterns in the transport term. The OH concentration, which is proportional to the intensity of the~~  
739 ~~sink term, is also important. We have shown that OH concentrations are partially responsible for an important drop~~  
740 ~~in NO<sub>x</sub> emissions in the winter of 2019/2020 that may be unrealistic. Because this decrease is largely due to variations~~  
741 ~~in OH concentrations provided by CAMS, whose reliability has been evaluated for Riyadh, then the transposability~~  
742 ~~hypothesis between Riyadh and Egypt may be subject to wider discussion. A better understanding of OH levels in~~  
743 ~~Egypt, supported by in-situ measurements, might answer these questions and allow to improve our model. further~~  
744 ~~discussion.~~

## 745 5 Conclusions

746 In this study, we investigated the potential of a top-down model of NO<sub>x</sub> emissions based on TROPOMI retrievals  
747 at high resolution over Egypt. The model is based on the study of a transport term and a sink term that requires  
748 different parameters to be calculated. Among those parameters, the concentration in OH, involved in the calculation  
749 of the NO<sub>2</sub> mixed lifetime, is of fundamental importance. The comparison between ~~the two ways of calculating the~~  
750 ~~lifetime of NO<sub>2</sub> shows that lifetimes derived from OH concentrations and NO<sub>2</sub> lifetimes derived from EMG function~~  
751  ~~fittings of line density profiles shows that the~~ OH concentration provided by CAMS ~~data~~ is reasonably reliable for the

752 country. Parameters are ~~therefore~~ taken in the first 200 m of the planetary boundary layer, because it is where OH  
753 shows the best consistency. However, the vertical sensitivity linked to this parameters remains high. Results illustrate  
754 the importance of the transport term at local scale, which is of the same order of magnitude as the sink term above  
755 large cities and industrial facilities; it ceases to be relevant only at the ~~country's scale~~ scale of the whole country. The  
756 top-down model is able to characterise declines in human activities ~~, whether they are~~ due to restrictions during the  
757 COVID-19 pandemic or to Friday rest. It also estimates higher emissions during summer. These high emissions ~~might~~  
758 may be interpreted by a higher consumption of electricity driven by air-conditioning during hot days, but it remains  
759 unclear whether this pattern clearly reproduces changes in human activity, in particular because the ~~different~~  
760 inventories show different seasonalities. These inventories also differ in the amount of total emissions: the average  
761 value for TROPOMI-derived NO<sub>x</sub> emissions ~~are 25.0~~ is 7.0% higher than ~~CAMS-CAMS-GLOB-ANT v4.2~~  
762 estimates. This discrepancy could be ~~solved~~ resolved by comparing the results of the model and inventory estimates to industrial  
763 production or electricity consumption data at the scale of countries or regions.

764 This study demonstrates the potential of TROPOMI data for evaluating NO<sub>x</sub> emissions in the ~~EMME~~ Middle East  
765 region. More generally, it demonstrates the importance of the contribution of independent observation systems to  
766 overcome the weaknesses of emission inventories, provided that the local chemistry is well understood and modelled.  
767 The development of similar applications for different species is likely to allow a better monitoring of global anthro-  
768 pogenic emissions, therefore helping companies and countries to report their ~~anthropogenic~~ emissions of air pollutants  
769 and greenhouse gases as part of their strategies and obligations to tackle air pollution issues and climate change.

#### 770 **Data availability.**

771 TROPOMI product: <http://www.tropomi.eu/data-products/data-access>  
772 CAMS NRT: <https://ads.atmosphere.copernicus.eu/cdsapp!/dataset/cams-global-atmospheric-composition-forecasts>  
773 ERA5 reanalysis: <https://cds.climate.copernicus.eu/cdsapp!/dataset/reanalysis-era5-pressure-levels-monthly-means>  
774 Global Rural-Urban Mapping Project (GRUMP): <https://sedac.ciesin.columbia.edu/data/collection/grump-v1>  
775 Oil and gas power plants: <http://globalenergyobservatory.org/>  
776 Industrial facilities: <https://www.industryabout.com>  
777 Flaring sites: [https://eogdata.mines.edu/download\\_global\\_flare.html](https://eogdata.mines.edu/download_global_flare.html)  
778 CAMS-GLOB-ANT\_v4.2: <https://permalink.aeris-data.fr/CAMS-GLOB-ANT>  
779 EDGARv5.0: [https://edgar.jrc.ec.europa.eu/dataset\\_ap50](https://edgar.jrc.ec.europa.eu/dataset_ap50)

780 **Competing interests.** The authors declare that they have no conflict of interest.

781 **Acknowledgements.** The authors would like to thank Steven J. Davis (University of California, Irvine) and Dan  
782 Tong (Tsinghua University) for their contribution to the construction of our emitters database.

783 **Financial support.** This study has been funded by the European Union's Horizon 2020 research and innovation  
784 programme under grant agreement N° 856612 (EMME-CARE).

## 785 **References**

- 786 [1] A. Baklanov, L. T. Molina, and M. Gauss, "Megacities, air quality and climate," *Atmospheric Environment*,  
787 vol. 126, pp. 235–249, 2016.
- 788 [2] L. Tang, X. Xue, M. Jia, H. Jing, T. Wang, R. Zhen, M. Huang, J. Tian, J. Guo, L. Li, *et al.*, "Iron and steel  
789 industry emissions and contribution to the air quality in China," *Atmospheric Environment*, vol. 237, p. 117668,  
790 2020.
- 791 [3] H. C. Kim, C. Bae, M. Bae, O. Kim, B.-U. Kim, C. Yoo, J. Park, J. Choi, J.-b. Lee, B. Lefer, *et al.*, "Space-Borne  
792 monitoring of NO<sub>x</sub> emissions from cement kilns in South Korea," *Atmosphere*, vol. 11, no. 8, p. 881, 2020.
- 793 [4] A. Singh and M. Agrawal, "Acid rain and its ecological consequences," *Journal of Environmental Biology*, vol. 29,  
794 no. 1, p. 15, 2007.

- 795 [5] U. EPA, “Integrated science assessment for oxides of nitrogen—health criteria,” *US Environmental Protection*  
796 *Agency, Washington, DC [Google Scholar]*, 2016.
- 797 [6] M. Crippa, G. Janssens-Maenhout, F. Dentener, D. Guizzardi, K. Sindelarova, M. Muntean, R. Van Dingenen,  
798 and C. Granier, “Forty years of improvements in European air quality: regional policy-industry interactions with  
799 global impacts,” *Atmospheric Chemistry and Physics*, vol. 16, no. 6, pp. 3825–3841, 2016.
- 800 [7] A. El-Magd, N. Zanaty, E. M. Ali, H. Irie, A. I. Abdelkader, *et al.*, “Investigation of aerosol climatology, optical  
801 characteristics and variability over Egypt based on satellite observations and in-situ measurements,” *Atmosphere*,  
802 vol. 11, no. 7, p. 714, 2020.
- 803 [8] UNEP (United Nations Environment Programme), “Air quality policies in Egypt,” 2015.
- 804 [9] B. Xue and W. Ren, “China’s uncertain CO<sub>2</sub> emissions,” *Nature Climate Change*, vol. 2, no. 11, pp. 762–762,  
805 2012.
- 806 [10] C. Leue, M. Wenig, T. Wagner, O. Klimm, U. Platt, and B. Jähne, “Quantitative analysis of NO<sub>x</sub> emissions from  
807 global ozone Monitoring Experiment satellite image sequences,” *Journal of Geophysical Research: Atmospheres*,  
808 vol. 106, no. D6, pp. 5493–5505, 2001.
- 809 [11] R. V. Martin, D. J. Jacob, K. Chance, T. P. Kurosu, P. I. Palmer, and M. J. Evans, “Global inventory of nitrogen  
810 oxide emissions constrained by space-based observations of NO<sub>2</sub> columns,” *Journal of Geophysical Research:*  
811 *Atmospheres*, vol. 108, no. D17, 2003.
- 812 [12] B. Mijling and R. Van Der A, “Using daily satellite observations to estimate emissions of short-lived air pollutants  
813 on a mesoscopic scale,” *Journal of Geophysical Research: Atmospheres*, vol. 117, no. D17, 2012.
- 814 [13] B. de Foy, Z. Lu, D. G. Streets, L. N. Lamsal, and B. N. Duncan, “Estimates of power plant NO<sub>x</sub> emissions and  
815 lifetimes from OMI NO<sub>2</sub> satellite retrievals,” *Atmospheric Environment*, vol. 116, pp. 1–11, 2015.
- 816 [14] D. L. Goldberg, Z. Lu, D. G. Streets, B. de Foy, D. Griffin, C. A. McLinden, L. N. Lamsal, N. A. Krotkov, and  
817 H. Eskes, “Enhanced Capabilities of TROPOMI NO<sub>2</sub>: Estimating NO<sub>x</sub> from North American Cities and Power  
818 Plants,” *Environmental science & technology*, vol. 53, no. 21, pp. 12594–12601, 2019.
- 819 [15] S. Beirle, C. Borger, S. Dörner, A. Li, Z. Hu, F. Liu, Y. Wang, and T. Wagner, “Pinpointing nitrogen oxide  
820 emissions from space,” *Science advances*, vol. 5, no. 11, p. eaax9800, 2019.
- 821 [16] A. Lorente, K. Boersma, H. Eskes, J. Veefkind, J. Van Geffen, M. De Zeeuw, H. D. van der Gon, S. Beirle, and  
822 M. Krol, “Quantification of nitrogen oxides emissions from build-up of pollution over Paris with TROPOMI,”  
823 *Scientific reports*, vol. 9, no. 1, pp. 1–10, 2019.
- 824 [17] K. Lange, A. Richter, and J. P. Burrows, “Variability of nitrogen oxide emission fluxes and lifetimes estimated  
825 from Sentinel-5P TROPOMI observations,” *Atmospheric Chemistry and Physics Discussions*, pp. 1–32, 2021.
- 826 [18] J. Veefkind, I. Aben, K. McMullan, H. Förster, J. De Vries, G. Otter, J. Claas, H. Eskes, J. De Haan, Q. Kleipool,  
827 *et al.*, “TROPOMI on the ESA Sentinel-5 Precursor: A GMES mission for global observations of the atmospheric  
828 composition for climate, air quality and ozone layer applications,” *Remote sensing of environment*, vol. 120,  
829 pp. 70–83, 2012.
- 830 [19] S. Lama, S. Houweling, K. F. Boersma, H. Eskes, I. Aben, H. A. Denier van der Gon, M. C. Krol, H. Dol-  
831 man, T. Borsdorff, and A. Lorente, “Quantifying burning efficiency in megacities using the NO<sub>2</sub>/CO ratio from  
832 the Tropospheric Monitoring Instrument (TROPOMI),” *Atmospheric Chemistry and Physics*, vol. 20, no. 17,  
833 pp. 10295–10310, 2020.
- 834 [20] H. Eskes, K. Eichmann, J. Lambert, D. Loyola, J. Veefkind, A. Dehn, and C. Zehner, “S5P Mission Performance  
835 Centre Nitrogen Dioxide [L2\_NO2] readme,” *Royal Netherlands Meteorological Institute (KNMI) De Bilt, the*  
836 *Netherlands, version*, vol. 1, no. 00, 2019.
- 837 [21] H. Hersbach, B. Bell, P. Berrisford, S. Hirahara, A. Horányi, J. Muñoz-Sabater, J. Nicolas, C. Peubey, R. Radu,  
838 D. Schepers, *et al.*, “The ERA5 global reanalysis,” *Quarterly Journal of the Royal Meteorological Society*, vol. 146,  
839 no. 730, pp. 1999–2049, 2020.

- 840 [22] V. Huijnen, H. Eskes, A. Wagner, M. Schulz, Y. Christophe, M. Ramonet, S. Basart, A. Benedic-  
841 tow, A.-M. Blechschmidt, S. Chabrillat, *et al.*, “Validation report of the CAMS near-real-time global at-  
842 mospheric composition service: System evolution and performance statistics. Status up to 1 June 2016;  
843 [https://pure.mpg.de/rest/items/item\\_2441827/component/file\\_2441834/content](https://pure.mpg.de/rest/items/item_2441827/component/file_2441834/content),” 2016.
- 844 [23] J. H. Seinfeld, “Urban air pollution: state of the science,” *Science*, vol. 243, no. 4892, pp. 745–752, 1989.
- 845 [24] J. A. Logan, M. J. Prather, S. C. Wofsy, and M. B. McElroy, “Tropospheric chemistry: a global perspective,”  
846 *Journal of Geophysical Research: Oceans*, vol. 86, no. C8, pp. 7210–7254, 1981.
- 847 [25] H. Levy, “Normal atmosphere: Large radical and formaldehyde concentrations predicted,” *Science*, vol. 173,  
848 no. 3992, pp. 141–143, 1971.
- 849 [26] L. Valin, A. Russell, R. Hudman, and R. Cohen, “Effects of model resolution on the interpretation of satellite  
850 NO<sub>2</sub> observations,” *Atmospheric Chemistry and Physics*, vol. 11, no. 22, pp. 11647–11655, 2011.
- 851 [27] J. Lelieveld, S. Gromov, A. Pozzer, and D. Taraborrelli, “Global tropospheric hydroxyl distribution, budget and  
852 reactivity,” *Atmospheric Chemistry and Physics*, vol. 16, no. 19, pp. 12477–12493, 2016.
- 853 [28] M. Li, E. Karu, C. Brenninkmeijer, H. Fischer, J. Lelieveld, and J. Williams, “Tropospheric OH and stratospheric  
854 OH and Cl concentrations determined from CH<sub>4</sub>, CH<sub>3</sub>Cl, and SF<sub>6</sub> measurements,” *NPJ Climate and Atmospheric  
855 Science*, vol. 1, no. 1, pp. 1–7, 2018.
- 856 [29] G. M. Wolfe, J. M. Nicely, J. M. S. Clair, T. F. Hanisco, J. Liao, L. D. Oman, W. B. Brune, D. Miller, A. Thames,  
857 G. G. Abad, *et al.*, “Mapping hydroxyl variability throughout the global remote troposphere via synthesis of  
858 airborne and satellite formaldehyde observations,” *Proceedings of the National Academy of Sciences*, vol. 116,  
859 no. 23, pp. 11171–11180, 2019.
- 860 [30] J. Burkholder, S. Sander, J. Abbatt, J. Barker, C. Cappa, J. Crounse, T. Dibble, R. Huie, C. Kolb, M. Kurylo,  
861 *et al.*, “Chemical kinetics and photochemical data for use in atmospheric studies; evaluation number 19,” tech.  
862 rep., Pasadena, CA: Jet Propulsion Laboratory, National Aeronautics and Space . . . , 2020.
- 863 [31] K. Boersma, H. Eskes, E. Meijer, and H. Kelder, “Estimates of lightning NO<sub>x</sub> production from some satellite  
864 observations,” *Atmospheric Chemistry and Physics*, vol. 5, no. 9, pp. 2311–2331, 2005.
- 865 [32] J. Yienger and H. Levy, “Empirical model of global soil-biogenic NO<sub>x</sub> emissions,” *Journal of Geophysical Research:  
866 Atmospheres*, vol. 100, no. D6, pp. 11447–11464, 1995.
- 867 [33] J. J. Hoelzemann, M. G. Schultz, G. P. Brasseur, C. Granier, and M. Simon, “Global wildland fire emission model  
868 (GWEM): Evaluating the use of global area burnt satellite data,” *Journal of Geophysical Research: Atmospheres*,  
869 vol. 109, no. D14, 2004.
- 870 [34] D. H. Ehhalt, F. Rohrer, and A. Wahner, “Sources and distribution of NO<sub>x</sub> in the upper troposphere at northern  
871 mid-latitudes,” *Journal of Geophysical Research: Atmospheres*, vol. 97, no. D4, pp. 3725–3738, 1992.
- 872 [35] L. Jaeglé, L. Steinberger, R. V. Martin, and K. Chance, “Global partitioning of NO<sub>x</sub> sources using satellite  
873 observations: Relative roles of fossil fuel combustion, biomass burning and soil emissions,” *Faraday discussions*,  
874 vol. 130, pp. 407–423, 2005.
- 875 [36] J.-F. Müller and T. Stavrou, “Inversion of CO and NO<sub>x</sub> emissions using the adjoint of the images model,”  
876 *Atmospheric Chemistry and Physics*, vol. 5, no. 5, pp. 1157–1186, 2005.
- 877 [37] J.-T. Lin, “Satellite constraint for emissions of nitrogen oxides from anthropogenic, lightning and soil sources over  
878 East China on a high-resolution grid,” *Atmospheric Chemistry and Physics*, vol. 12, no. 6, pp. 2881–2898, 2012.
- 879 [38] CIESIN, “CIESIN. Global Rural-Urban Mapping Project, Version 1 (GRUMPv1). Center for International Earth  
880 Science Information Network - CIESIN - Columbia University, International Food Policy Research Institute -  
881 IFPRI, The World Bank, and Centro Internacional de Agricultura Tropical - CIAT. 2011, Palisades, NY: NASA  
882 Socioeconomic Data and Applications Center (SEDAC),” 2019.
- 883 [39] C. D. Elvidge, M. Zhizhin, K. Baugh, F.-C. Hsu, and T. Ghosh, “Methods for global survey of natural gas flaring  
884 from visible infrared imaging radiometer suite data,” *Energies*, vol. 9, no. 1, p. 14, 2016.

- 885 [40] C. Granier, S. Darras, H. D. van der Gon, D. Jana, N. Elguindi, G. Bo, G. Michael, G. Marc, J.-P. Jalkanen,  
886 J. Kuenen, *et al.*, *The Copernicus atmosphere monitoring service global and regional emissions (April 2019*  
887 *version)*. PhD thesis, Copernicus Atmosphere Monitoring Service, 2019.
- 888 [41] M. Crippa, D. Guizzardi, M. Muntean, E. Schaaf, E. Solazzo, F. Monforti-Ferrario, J. Olivier, and E. Vignati,  
889 “Fossil CO<sub>2</sub> emissions of all world countries,” *Luxembourg: European Commission*, pp. 1–244, 2020.
- 890 [42] R. M. Hoesly, S. J. Smith, L. Feng, Z. Klimont, G. Janssens-Maenhout, T. Pitkanen, J. J. Seibert, L. Vu, R. J.  
891 Andres, R. M. Bolt, *et al.*, “Historical (1750–2014) anthropogenic emissions of reactive gases and aerosols from  
892 the community emissions data system (CEDS),” *Geoscientific Model Development*, vol. 11, no. 1, pp. 369–408,  
893 2018.
- 894 [43] G. Janssens-Maenhout, M. Crippa, D. Guizzardi, M. Muntean, E. Schaaf, F. Dentener, P. Bergamaschi,  
895 V. Pagliari, J. G. Olivier, J. A. Peters, *et al.*, “Edgar v4. 3.2 global atlas of the three major greenhouse gas  
896 emissions for the period 1970–2012,” *Earth System Science Data*, vol. 11, no. 3, pp. 959–1002, 2019.
- 897 [44] K. Boersma, H. Eskes, and E. Brinksma, “Error analysis for tropospheric NO<sub>2</sub> retrieval from space,” *Journal of*  
898 *Geophysical Research: Atmospheres*, vol. 109, no. D4, 2004.
- 899 [45] A. Lorente, K. Folkert Boersma, H. Yu, S. Dörner, A. Hilboll, A. Richter, M. Liu, L. N. Lamsal, M. Barkley,  
900 I. D. Smedt, *et al.*, “Structural uncertainty in air mass factor calculation for NO<sub>2</sub> and HCHO satellite retrievals,”  
901 *Atmospheric Measurement Techniques*, vol. 10, no. 3, pp. 759–782, 2017.
- 902 [46] S. Sander, R. Friedl, J. Abbatt, J. Barker, J. Burkholder, D. Golden, C. Kolb, M. Kurylo, G. Moortgat, P. Wine,  
903 *et al.*, “Chemical kinetics and photochemical data for use in atmospheric studies, jpl publication 10-6,” *Evaluation*,  
904 no. 17, 2011.
- 905 [47] B. A. Nault, C. Garland, P. J. Wooldridge, W. H. Brune, P. Campuzano-Jost, J. D. Crouse, D. A. Day, J. Dibb,  
906 S. R. Hall, L. G. Huey, *et al.*, “Observational constraints on the oxidation of NO<sub>x</sub> in the upper troposphere,” *The*  
907 *Journal of Physical Chemistry A*, vol. 120, no. 9, pp. 1468–1478, 2016.
- 908 [48] T. Stavrou, J.-F. Müller, K. Boersma, R. Van Der A, J. Kurokawa, T. Ohara, and Q. Zhang, “Key chemical  
909 NO<sub>x</sub> sink uncertainties and how they influence top-down emissions of nitrogen oxides,” *Atmospheric Chemistry*  
910 *and Physics*, vol. 13, no. 17, pp. 9057–9082, 2013.
- 911 [49] H. Fang, F. Baret, S. Plummer, and G. Schaepman-Strub, “An overview of global leaf area index (LAI): Methods,  
912 products, validation, and applications,” *Reviews of Geophysics*, vol. 57, no. 3, pp. 739–799, 2019.
- 913 [50] E. R. Delaria, B. K. Place, A. X. Liu, and R. C. Cohen, “Laboratory measurements of stomatal NO<sub>2</sub> deposition  
914 to native california trees and the role of forests in the NO<sub>x</sub> cycle,” *Atmospheric Chemistry and Physics*, vol. 20,  
915 no. 22, pp. 14023–14041, 2020.
- 916 [51] N. Sobanski, J. Thieser, J. Schuladen, C. Sauvage, W. Song, J. Williams, J. Lelieveld, and J. N. Crowley, “Day  
917 and night-time formation of organic nitrates at a forested mountain site in south-west germany,” *Atmospheric*  
918 *Chemistry and Physics*, vol. 17, no. 6, pp. 4115–4130, 2017.
- 919 [52] A. Guenther, T. Karl, P. Harley, C. Wiedinmyer, P. I. Palmer, and C. Geron, “Estimates of global terrestrial  
920 isoprene emissions using megan (model of emissions of gases and aerosols from nature),” *Atmospheric Chemistry*  
921 *and Physics*, vol. 6, no. 11, pp. 3181–3210, 2006.
- 922 [53] P. S. Romer Present, A. Zare, and R. C. Cohen, “The changing role of organic nitrates in the removal and  
923 transport of NO<sub>x</sub>,” *Atmospheric Chemistry and Physics*, vol. 20, no. 1, pp. 267–279, 2020.
- 924 [54] N. Butkovskaya, A. Kukui, N. Pouvesle, and G. Le Bras, “Formation of nitric acid in the gas-phase HO<sub>2</sub>+NO  
925 reaction: Effects of temperature and water vapor,” *The Journal of Physical Chemistry A*, vol. 109, no. 29,  
926 pp. 6509–6520, 2005.
- 927 [55] N. Butkovskaya, M.-T. Rayez, J.-C. Rayez, A. Kukui, and G. Le Bras, “Water vapor effect on the HNO<sub>3</sub> yield in  
928 the HO<sub>2</sub>+NO reaction: experimental and theoretical evidence,” *The Journal of Physical Chemistry A*, vol. 113,  
929 no. 42, pp. 11327–11342, 2009.
- 930 [56] W. Moxim, H. Levy, and P. Kasibhatla, “Simulated global tropospheric PAN: Its transport and impact on NO<sub>x</sub>,”  
931 *Journal of Geophysical Research: Atmospheres*, vol. 101, no. D7, pp. 12621–12638, 1996.



- 932 [57] C. A. Longfellow, A. Ravishankara, and D. R. Hanson, "Reactive uptake on hydrocarbon soot: Focus on NO<sub>2</sub>,"  
933 *Journal of Geophysical Research: Atmospheres*, vol. 104, no. D11, pp. 13833–13840, 1999.
- 934 [58] N. Friedrich, P. Eger, J. Shenolikar, N. Sobanski, J. Schuladen, D. Dienhart, B. Hottmann, I. Tadic, H. Fischer,  
935 M. Martinez, *et al.*, "Reactive nitrogen around the arabian peninsula and in the mediterranean sea during the  
936 2017 AQABA ship campaign," *Atmospheric Chemistry and Physics*, vol. 21, no. 10, pp. 7473–7498, 2021.
- 937 [59] E. Fischer, D. J. Jacob, R. M. Yantosca, M. P. Sulprizio, D. Millet, J. Mao, F. Paulot, H. Singh, A. Roiger,  
938 L. Ries, *et al.*, "Atmospheric peroxyacetyl nitrate (PAN): a global budget and source attribution," *Atmospheric*  
939 *Chemistry and Physics*, vol. 14, no. 5, pp. 2679–2698, 2014.
- 940 [60] S. Attia, A. Evrard, and E. Gratia, "Development of benchmark models for the Egyptian residential buildings  
941 sector," *Applied Energy*, vol. 94, pp. 270–284, 2012.
- 942 [61] EEHC, "Egyptian Electricity Holding Company annual report 2019/2020," 2021.
- 943 [62] F. Rohrer and H. Berresheim, "Strong correlation between levels of tropospheric hydroxyl radicals and solar  
944 ultraviolet radiation," *Nature*, vol. 442, no. 7099, pp. 184–187, 2006.
- 945 [63] S. Beirle, K. F. Boersma, U. Platt, M. G. Lawrence, and T. Wagner, "Megacity emissions and lifetimes of nitrogen  
946 oxides probed from space," *Science*, vol. 333, no. 6050, pp. 1737–1739, 2011.
- 947 [64] L. Valin, A. Russell, and R. Cohen, "Variations of OH radical in an urban plume inferred from NO<sub>2</sub> column  
948 measurements," *Geophysical Research Letters*, vol. 40, no. 9, pp. 1856–1860, 2013.
- 949 [65] M. Filioglou, E. Giannakaki, J. Backman, J. Kesti, A. Hirsikko, R. Engelmann, E. O'Connor, J. T. Leskinen,  
950 X. Shang, H. Korhonen, *et al.*, "Optical and geometrical aerosol particle properties over the United Arab Emirates,"  
951 *Atmospheric Chemistry and Physics*, vol. 20, no. 14, pp. 8909–8922, 2020.
- 952 [66] M. Khoder, "Diurnal, seasonal and weekdays-weekends variations of ground level ozone concentrations in an  
953 urban area in greater cairo," *Environmental Monitoring and Assessment*, vol. 149, no. 1, pp. 349–362, 2009.
- 954 [67] T. Graedel, L. Farrow, and T. Weber, "Kinetic studies of the photochemistry of the urban troposphere," *Atmo-*  
955 *spheric Environment (1967)*, vol. 10, no. 12, pp. 1095–1116, 1976.
- 956 [68] J. H. Seinfeld and S. N. Pandis, "Atmospheric chemistry and physics from air pollution to climate change," 2006.
- 957 [69] S. Beirle, C. Borger, S. Dörner, H. Eskes, V. Kumar, A. de Laat, and T. Wagner, "Catalog of NO<sub>x</sub> emissions  
958 from point sources as derived from the divergence of the NO<sub>2</sub> flux for TROPOMI," *Earth System Science Data*,  
959 vol. 13, no. 6, pp. 2995–3012, 2021.
- 960 [70] T. Stavrou, J.-F. Müller, M. Bauwens, K. Boersma, and J. van Geffen, "Satellite evidence for changes in the  
961 NO<sub>2</sub> weekly cycle over large cities," *Scientific reports*, vol. 10, no. 1, pp. 1–9, 2020.
- 962 [71] U. IEA, "Global energy review 2020," *Ukraine.[Online] https://www.iea.org/countries/ukraine [Accessed: 2020-*  
963 *09-10]*, 2020.
- 964 [72] Z. S. Venter, K. Aunan, S. Chowdhury, and J. Lelieveld, "COVID-19 lockdowns cause global air pollution declines,"  
965 *Proceedings of the National Academy of Sciences*, vol. 117, no. 32, pp. 18984–18990, 2020.
- 966 [73] M. Bauwens, S. Compornolle, T. Stavrou, J.-F. Müller, J. Van Gent, H. Eskes, P. F. Levelt, R. van der A,  
967 J. Veefkind, J. Vlietinck, *et al.*, "Impact of coronavirus outbreak on NO<sub>2</sub> pollution assessed using TROPOMI and  
968 OMI observations," *Geophysical Research Letters*, vol. 47, no. 11, p. e2020GL087978, 2020.
- 969 [74] J. Barré, H. Petetin, A. Colette, M. Guevara, V.-H. Peuch, L. Rouil, R. Engelen, A. Inness, J. Flemming,  
970 C. Pérez García-Pando, *et al.*, "Estimating lockdown-induced european NO<sub>2</sub> changes using satellite and surface  
971 observations and air quality models," *Atmospheric Chemistry and Physics*, vol. 21, no. 9, pp. 7373–7394, 2021.
- 972 [75] G. I. Gkatzelis, J. B. Gilman, S. S. Brown, H. Eskes, A. R. Gomes, A. C. Lange, B. C. McDonald, J. Peischl,  
973 A. Petzold, C. R. Thompson, *et al.*, "The global impacts of COVID-19 lockdowns on urban air pollution: a critical  
974 review and recommendations," *Elementa: Science of the Anthropocene*, vol. 9, no. 1, 2021.

- 975 [76] T. Hale, N. Angrist, R. Goldszmidt, B. Kira, A. Petherick, T. Phillips, S. Webster, E. Cameron-Blake, L. Hallas,  
976 S. Majumdar, *et al.*, “A global panel database of pandemic policies (oxford covid-19 government response tracker),”  
977 *Nature Human Behaviour*, vol. 5, no. 4, pp. 529–538, 2021.
- 978 [77] M. M. El-Sheekh and I. A. Hassan, “Lockdowns and reduction of economic activities during the COVID-19  
979 pandemic improved air quality in Alexandria, Egypt,” *Environmental Monitoring and Assessment*, vol. 193,  
980 no. 1, pp. 1–7, 2021.
- 981 [78] I. Abou El-Magd and N. Zanaty, “Impacts of short-term lockdown during COVID-19 on air quality in Egypt,”  
982 *The Egyptian Journal of Remote Sensing and Space Science*, 2020.
- 983 [79] L. Abdallah and T. El-Shennawy, “Evaluation of CO2 emission from Egypt’s future power plants,” *Euro-  
984 Mediterranean Journal for Environmental Integration*, vol. 5, no. 3, pp. 1–8, 2020.
- 985 [80] A. M. A. H. Elharidi, P. G. Tuohy, and M. Teamah, “Facing the growing problem of the electric power consumption  
986 in Egyptian residential building using building performance simulation program,” in *Building simulation Cairo  
987 2013 conference*, 2013.
- 988 [81] M. M. Nassief, “Evaluation of electricity consumption of a residential flat in egypt,” *American Journal of Electrical  
989 Power and Energy Systems*, vol. 3, no. 2, pp. 7–44, 2014.
- 990 [82] S. M. Wahba, B. A. Kamel, K. M. Nassar, and A. S. Abdelsalam, “Effectiveness of green roofs and green walls on  
991 energy consumption and indoor comfort in arid climates,” *Civil Engineering Journal*, vol. 4, no. 10, pp. 2284–2295,  
992 2018.
- 993 [83] S. Compernelle *et al.*, “S5P MPC VDAF validation web article: Nitrogen dioxide,” tech. rep., S5P-MPC-VDAF-  
994 WVA-L2\_NO2\_20180904, 2018.
- 995 [84] J. J. Coburn, “Assessing wind data from reanalyses for the upper midwest,” *Journal of Applied Meteorology and  
996 Climatology*, vol. 58, no. 3, pp. 429–446, 2019.
- 997 [85] V. Huijnen, A. Pozzer, J. Arteta, G. Brasseur, I. Bouarar, S. Chabrillat, Y. Christophe, T. Doumbia, J. Flemming,  
998 J. Guth, *et al.*, “Quantifying uncertainties due to chemistry modelling—evaluation of tropospheric composition  
999 simulations in the CAMS model (cycle 43r1),” *Geoscientific Model Development*, vol. 12, no. 4, pp. 1725–1752,  
1000 2019.

1001